



HAL
open science

A Role for the Mre11-Rad50-Xrs2 Complex in Gene Expression and Chromosome Organization

Romain Forey, Antoine Barthe, Mireille Tittel-Elmer, Maxime Wery, Marie-Bénédicte Barrault, Cécile Ducrot, Andrew Seeber, Nils Krietenstein, Ugo Szachnowski, Magdalena Skrzypczak, et al.

► **To cite this version:**

Romain Forey, Antoine Barthe, Mireille Tittel-Elmer, Maxime Wery, Marie-Bénédicte Barrault, et al.. A Role for the Mre11-Rad50-Xrs2 Complex in Gene Expression and Chromosome Organization. *Molecular Cell*, 2020, 10.1016/j.molcel.2020.11.010 . hal-03048169

HAL Id: hal-03048169

<https://hal.science/hal-03048169>

Submitted on 25 Aug 2023

HAL is a multi-disciplinary open access archive for the deposit and dissemination of scientific research documents, whether they are published or not. The documents may come from teaching and research institutions in France or abroad, or from public or private research centers.

L'archive ouverte pluridisciplinaire **HAL**, est destinée au dépôt et à la diffusion de documents scientifiques de niveau recherche, publiés ou non, émanant des établissements d'enseignement et de recherche français ou étrangers, des laboratoires publics ou privés.

A role for the Mre11–Rad50–Xrs2 complex in gene expression and chromosome organization

Romain Forey¹, Antoine Barthe¹, Mireille Tittel-Elmer², Maxime Wery³, Marie-Bénédicte Barrault⁴, Cécile Ducrot⁵, Andrew Seeber⁶, Nils Krietenstein⁷, Ugo Szachnowski³, Magdalena Skrzypczak⁸, Krzysztof Ginalski⁸, Maga Rowicka⁹, Jennifer Cobb², Oliver J. Rando⁷, Julie Soutourina⁴, Michel Werner¹⁰, Karine Dubrana⁵, Susan M. Gasser¹¹, Antonin Morillon³, Philippe Pasero¹, Armelle Lengronne^{1*} and Jérôme Poli^{1,12*}

1) Institut de Génétique Humaine, CNRS, Université de Montpellier, 34396, Montpellier, France

2) Departments of Biochemistry & Molecular Biology and Oncology, Robson DNA Science Centre, Arnie Charbonneau Cancer Institute, Cumming School of Medicine, University of Calgary, Calgary, Alberta, Canada.

3) Institut Curie, PSL Research University, CNRS UMR 3244, ncRNA, Epigenetic and Genome Fluidity, Université Pierre et Marie Curie, 26 rue d'Ulm, 75248, Paris, France.

4) Université Paris-Saclay, CEA, CNRS, Institute for Integrative Biology of the Cell (I2BC), 91198 Gif-sur-Yvette, France.

5) Institute of Molecular & Cellular Radiobiology, Commissariat à l'Énergie Atomique et aux Énergies Alternatives (CEA)/Direction de la Recherche Fondamentale (DRF), 92260 Fontenay-aux-Roses Cedex, France

6) Center for Advanced Imaging, Harvard University, Cambridge, MA, 02138, USA

7) Department of Biochemistry & Molecular Pharmacology, University of Massachusetts Medical School, Worcester, MA 01605, USA

8) Laboratory of Bioinformatics & Systems Biology, Centre of New Technologies, University of Warsaw, Zwirki i Wigury 93, 02-089 Warsaw, Poland.

9) Department of Biochemistry & Molecular Biology, University of Texas Medical Branch at Galveston, Galveston, TX, USA.

10) Institut Jacques Monod, CNRS UMR 7592, Université Paris Diderot, Sorbonne Paris Cité, 75013 Paris, France.

11) University of Basel & Friedrich Miescher Institute for Biomedical Research, Faculty of Natural Sciences, Klingelbergstrasse 50, CH-4056 Basel, Switzerland

12) Lead Contact

*Corresponding authors: armelle.lengronne@igh.cnrs.fr ; jerome.poli@igh.cnrs.fr

Tel: +33 4 34 35 99 55

Fax: +33 4 34 35 99 01

Key words: MRX/N, Mediator, coding and non-coding transcription control, nuclear pore, chromosome organization, chromosomal interaction domains, chromosome folding.

Summary (129 words)

Mre11–Rad50–Xrs2 (MRX) is a highly conserved complex with key roles in various aspects of DNA repair. Here, we report a new function for MRX in limiting transcription in budding yeast. We show that MRX interacts physically and colocalizes on chromatin with the transcriptional co-regulator Mediator. MRX restricts transcription of coding and noncoding DNA by a mechanism that does not require the nuclease activity of Mre11. MRX is required to tether transcriptionally active loci to the nuclear pore complex (NPC) and also promotes large-scale gene–NPC interactions. Moreover, MRX-mediated chromatin anchoring to the NPC contributes to chromosome folding and helps to control gene expression. Together, these findings indicate that MRX has a role in transcription and chromosome organization that is distinct from its known function in DNA repair.

Introduction (1106 words)

Recent advances in genomics and high-throughput sequencing technologies have shown that transcription is not limited to annotated genes but is rather a pervasive process that initiates from proximal and distal regulatory sequences and occurs also on the antisense strand of genes (Tisseur et al., 2011). The resulting pervasive non-coding transcripts, unlike coding transcripts, are often unstable due to their rapid degradation by nuclear and cytoplasmic RNA surveillance systems. Thus, they are barely detectable in normal cells but they accumulate if the degradation machineries are inactivated. Although pervasive transcripts were initially grouped in respect to the pathway mediating their suppression, they are exclusively transcribed by RNAPII and often result from divergent transcription at 5' and 3' ends of genes (Jensen et al., 2013). In eukaryotes, promoters frequently display divergent transcription where a typical stable mRNA is generated toward the gene body and an unstable non-coding RNA is synthesized in the reverse direction away from the gene (Seila et al., 2009).

The structure of chromatin generally prevents transcription by limiting the accessibility of DNA sequences to the transcriptional machinery (Gasser and Laemmli, 1987). This default repressive status maintains a low level of expression genome-wide, except at sites where positive regulatory sequences promote the initiation of transcription. This chromatin-mediated transcriptional repression is relieved by chromatin remodelers and histone-modifying enzymes that alter nucleosome–DNA interactions (Petty and Pillus, 2013). This is particularly the case at promoter regions, where remodelers create and stabilize nucleosome-depleted regions unmasking binding sites for transcription activators and promoting assembly of the pre-initiation complex that binds RNA polymerase II (RNAPII) (Krietenstein et al., 2016; Li et al., 2007; Parnell et al., 2015). RNAPII activation requires the co-regulator called Mediator, a complex that transduces signals from distant, enhancer-bound activators to the machinery

at the transcription start site (TSS) (Soutourina, 2018). Mediator also facilitates efficient nuclear export of mRNAs through its interaction with the transcription-coupled export complex TREX2 (Jani et al., 2014; Schneider et al., 2015). The Mediator–TREX2 interaction anchors genes to the nuclear pore complex (NPC), also allowing optimal RNAPII loading and mRNA production (Schneider et al., 2015).

The gene–NPC interaction can also enhance transcription initiation by relieving transcriptional repression (Texari et al., 2013). Consistent with this, the NPC preferentially binds transcriptionally active genes (Capelson et al., 2010; Casolari et al., 2004; Liang et al., 2013). Also, inducible genes relocate from the interior of the nucleus to the NPC upon activation; in most cases, however, association with the NPC is not required for activation but, rather, fine-tunes the level of expression (Ahmed et al., 2010; Rohner et al., 2013; Schmid et al., 2006; Taddei et al., 2006a). In yeast, anchoring of the galactose-induced *GAL1-10* gene to the NPC (Cabal et al., 2006) is associated with large-scale repositioning of chromosomal regions to the nuclear periphery (Dultz et al., 2016). Mechanisms of gene recruitment to the NPC are not completely understood but involve physical interactions between transcription complexes and NPC components. The SAGA chromatin remodeler interacts with the NPC basket protein Mlp1 (Luthra et al., 2007), Mediator-TREX2 contacts the Nup1 subunit (Jani et al., 2014; Schneider et al., 2015) and the mRNA export receptor Mex67 associates with various NPC subunits (Dieppois et al., 2006). Gene-NPC anchoring is also controlled by *cis*-acting sequences in promoters which are recognized by specific transcription factors (Randise-Hinchliff et al., 2016).

Chromosomes are organized and folded into subnuclear compartments, with active domains preferentially localized in the nuclear interior or to the NPC in contrast with

repressed regions which are usually plastered against the inner nuclear membrane (Akhtar and Gasser, 2007). Chromosome regions in a domain preferentially self-interact over interactions with the neighboring domain. These contact domains are defined as topologically associating domains (TADs) or chromosomal interaction domains (CIDs) and conserved in many species (Szabo et al., 2019). TADs/CIDs are separated one from the other by boundary regions often found in active chromatin. Boundaries are defined by the strength of local insulation of a given domain with respect to neighboring domains. In *S. cerevisiae*, boundaries colocalize with highly expressed gene promoters, are enriched for the RSC chromatin remodeler and the cohesin loading factor Scc2 (Hsieh et al., 2015) whereas in mammals, most boundaries are enriched with CTCF and the structural maintenance of chromosome (SMC) cohesin complexes which are thought to promote the formation of chromosome loops (Fudenberg et al., 2017).

The Mre11–Rad50–Xrs2 (MRX) complex is a key factor in the DNA damage response in yeast, where it has both catalytic and structural roles. At DNA double-strand break (DSB)s, the Mre11 subunit, which is a nuclease, initiates DNA-end resection (Mimitou and Symington, 2008; Stracker and Petrini, 2011). The Xrs2 subunit acts as an interaction platform that brings together the various components of DNA repair foci and promotes checkpoint activation (Oh and Symington, 2018). In the functionally equivalent complex in human cells, Xrs2 is replaced by Nbs1. The resulting MRE11–RAD50–NBS1 (MRN) complex recruits RNAPII to DSBs, facilitating RNA synthesis, which is required locally during the repair process (Michelini et al., 2017). The Rad50 subunit is often considered a SMC-like factor due to its extensive structural homology with SMC proteins and the presence of an ATPase domain (Oh and Symington, 2018). The SMC family is crucial for long-range chromatin organization, chromosome segregation, condensation and repair (Uhlmann, 2016). Like SMC complexes, MRX forms ring-

shaped or higher order oligomeric structures able to hold together sister chromatids and DNA ends at DSBs (Hohl et al., 2011; Seeber et al., 2016). Besides its well-characterized functions in the DNA damage response, limited evidence suggests that MRX might be involved in other processes. For instance, long-range clustering of the yeast mating type loci (*HMR–HML*) is lost in *MRX* mutants (Kirkland and Kamakaka, 2013) and artificial tethering of Mre11 to DNA is sufficient to induce chromatin silencing of a reporter gene (Kirkland et al., 2015). The mechanism by which MRX/MRN executes these functions has remained largely unexplored.

Here, we investigate whether MRX plays a role in chromosome organization and genome expression in yeast. We find that MRX and Mediator colocalize to intergenic regions throughout the genome and interact physically during normal growth conditions. We also report that MRX limits both coding and pervasive non-coding transcription independently of the nuclease activity of Mre11. The MRX complex physically interacts with the NPC protein Nup60 and anchors several inducible loci to the NPC. In addition, we report that MRX not only governs interactions between inducible genes and the NPC but also mediates genome-wide anchoring of chromatin to the NPC. Lastly, we show that MRX's association with promoters contributes to chromosome folding by insulating CIDs. These findings indicate that the structural features of MRX mediate higher-order chromatin organization at the genome-wide level.

Results

The MRX complex binds to intergenic regions

Previous studies have reported that the MRX complex associates with sites of DNA damage (D'Amours and Jackson, 2002; Lisby and Rothstein, 2004; Seeber et al., 2016; Shroff et al., 2004) and with stalled replication forks (Delamarre et al., 2019; Tittel-Elmer et al., 2009, 2012), but the question of whether MRX might bind elsewhere in the genome when the DNA is intact has remained largely unexplored. To determine whether MRX binds chromatin in these circumstances, we analyzed the distribution of the HA-epitope tagged MRX subunit Rad50 by ChIP-seq in wild-type *S. cerevisiae* cells synchronized in G₁ phase with α -factor so there is no ongoing DNA replication. This analysis revealed that MRX binds chromatin at multiple sites in the genome of undamaged, non-replicating cells (**Figure 1A**). Computational 'peak-calling analysis using MACS2' was then applied to identify areas of the genome that were enriched with aligned reads in the Rad50 ChIP-seq analysis. Since ChIP experiments sometimes generate artifacts, ChIP signals from a control yeast strain lacking the HA-epitope tag and from loci prone to artifacts (Teytelman et al., 2013) were discarded (**Figure 1A**, asterisk). This approach identified 540 MRX-binding sites in intergenic regions surrounding ORFs or on gene body (**Table S1**); some of these sites were validated with a robust enrichment of Rad50 by ChIP-qPCR (**Figure 1B**). To test if these MRX-binding sites correspond to sites of spontaneous DNA lesions, we first compared the distribution of Rad50 by ChIP-seq analysis to that of γ -H2A, a marker of DNA breaks and replication stress (**Figure S1A**). Globally, the distributions of Rad50 and γ -H2A correlated negatively (**Figure S1B**): 90% of Rad50-enriched regions (488 out of 540) were devoid of γ -H2A signal (**Figure S1C and S1D**). Then, we performed a GFP-Tel1 ChIP-qPCR in G₁-arrested cells in wild-type and *ku70 Δ* cells. As expected, we could readily

recover Tel1 at eroded telomeres in the *ku70Δ* mutant but not at regular wild-type telomeres (**Figure S1E** and Hector *et al.* 2007). Tel1 did not accumulate either at active genes in G₁-arrested cells, regardless of the presence of Rad50 (**Figure S1E**). Lastly, we measured DSBs genome-wide in G₁-arrested cells using quantitative i-BLESS (immobilized Breaks Labeling, Enrichment on Streptavidin and next-generation Sequencing, (Biernacka *et al.*, 2018)). This analysis revealed that DSBs are very rare in G₁ cells (~1 DSB/cell) in comparison to S-phase cells (~15 DSBs/cell) or to cells exposed to genotoxic drugs such as hydroxyurea (~150 one-ended DSBs/cell) or zeocin (~8 DSBs/cell, **Figure S1F**). In addition, DSB occurrence was very similar between loci enriched (cluster 1) or not (cluster 2) in MRX and Mediator (**Figure S1G**). Together, these results indicate that the bulk of chromatin-bound Rad50 is not located at spontaneous DSBs in G₁-arrested cells.

To assess whether the MRX complex colocalizes with factors involved in transcription, we compared the distribution of the MRX subunit Rad50 to those of the Mediator subunit Med17 and the RNAPII subunit Rpb1, both components of the transcription machinery. First, we applied a MACS2 peak-calling analysis on the Med17 ChIP-seq which led to the identification of 728 areas of the genome that were enriched with the Mediator complex (Eyboulet *et al.*, 2013). Rad50-enriched regions overlapped 47.7% with Med17-enriched regions (**Figure 1A,C and Figure S1H**). Measuring the ChIP-seq enrichment of two Mediator subunits Med15 and Med17 at +/- 10 kb from Rad50 peaks shows that both complexes bind to the same DNA region (**Figure S1I**). Metaplots of the distribution of Rad50 at RNAPII genes revealed enrichment upstream of transcription start site (TSS)s – especially at TSSs enriched in Med17 – and around transcription termination site (TTS)s (**Figure 1D**). As both Mediator and MRX complexes are mostly found together at only a subset of ORFs, we next sought to determine the characteristics of these ORFs. Thus, we grouped ORFs by *k*-means clustering

($k=2$) on the Mediator subunit Med17 ChIP-seq levels (**Figure 1D**). One ORF cluster (C1, $n=656$, **Figure 1E** and **Table S2**) includes all detectable Med17-bound loci, it is highly enriched in Rad50 and Rpb1, and is characterized by a high mRNA level whereas the other cluster (C2, $n=3894$, **Figure 1E** and **Table S2**) is weakly enriched in the three factors and 1.6-fold lower in mRNA level compared to Cluster 1 (**Figure 1E**). These data indicate that MRX colocalizes with Mediator upstream of highly expressed RNAPII genes and is also present at TTSs.

Since MRX overlaps with Mediator at the promoters of many genes, we wondered whether these two complexes might interact physically. To address this possibility, we used a strain expressing HA-epitope tagged Mediator subunits Med17 or Med5 ([Eyboulet et al., 2015](#)) and FLAG-epitope-tagged Rad50. Immunoprecipitation of either of the tagged Mediator subunits co-immunoprecipitated Rad50–FLAG at well above control levels (Rad50–FLAG only strain, **Figure 1F**), independently of DNA (**Figure S1J**). These data indicate that these complexes interact physically and colocalize on chromatin at the promoters of highly expressed genes in G₁-phase cells.

MRX limits transcription of non-coding sequences

Mediator plays a key role in transcription by enabling assembly of the pre-initiation complex and controlling global expression of RNAPII-transcribed genes ([Eychenne et al., 2017](#)). Since we showed above that MRX interacts with Mediator, we wondered if MRX might also regulate transcription. To address this question, we performed strand-specific RNA-seq of G₁-arrested cells in which MRX was inactivated by deletion of MRE11 (*mre11Δ*) or RAD50 (*rad50Δ*) and compared the RNAs to those in wild-type cells. We then quantified differentially expressed mRNAs and pervasive long non-coding RNA (lncRNA)s including cryptic unstable transcript (CUT)s ([Neil et al., 2009](#); [Xu et al., 2009](#)), stable unannotated transcript (SUT)s ([Xu et al., 2009](#)),

Xrn1-sensitive unstable transcript (XUT)s (van Dijk et al., 2011; Wery et al., 2016) and divergent transcripts (Churchman and Weissman, 2011a; Marquardt et al., 2014). Comparative analysis of normalized read densities revealed a significant increase in the levels of lncRNAs and divergent ncRNAs in mutants lacking a functional MRX (*mre11Δ* and *rad50Δ*) when compared to wild-type cells (Figure 2A and S2A), regardless of ncRNA class (CUT, SUT, XUT or divergent Figure S2B). This is illustrated, for example, by the increased level of SUT743, which is transcribed from the *PRM1* locus on the RNA-seq heatmap profiles (Figure 2B). The increase in the levels of lncRNAs was confirmed by RT-qPCR analysis of a subset of lncRNAs (Figure S2C). An increase in mRNA levels was also observed in *rad50Δ* and *mre11Δ* cells, but the increase was smaller than that seen for lncRNAs (Figure 2A and S2A).

We quantified the fraction of transcripts whose expression was altered in *rad50Δ* and *mre11Δ* mutants compared to wild-type cells by using differential gene expression. This led to the identification of 939 and 723 transcripts differentially expressed in *rad50Δ* cells and in *mre11Δ* cells, respectively, compared to wild-type (Figure 2C and S2D). Consistent with the global analysis above, transcript levels mostly increased regardless of their class (mRNAs, divergent RNAs and lncRNAs) in *rad50Δ* cells and in *mre11Δ* cells, whereas the levels of a minority of transcripts decreased (Figure 2D, S2E, Table S3 and Table S4). Moreover, a smaller proportion of lncRNAs were upregulated in *mre11Δ* cells (5.6%) than in *rad50Δ* cells (10.4%) (Figure 2D and S2E). The transcriptomes of both deletion mutants were very similar, however, revealing an upregulation of steady-state transcription at a subset of loci (Figure S2F, S2G, Table S3 and Table S4). Together, these data support a role for the MRX complex in repressing transcription of protein-coding genes and limiting pervasive transcription.

The transcriptional repression and DNA repair functions of MRX are distinct

The MRX complex has both structural and catalytic activities: at DSBs and at collapsed DNA replication forks it holds sister chromatids together structurally while its nuclease activity promotes DNA end resection (Seeber et al., 2016; Tittel-Elmer et al., 2012). To determine whether MRX-mediated transcriptional repression requires the nuclease activity of Mre11, we analyzed the transcriptome in the nuclease-dead mutant *mre11-H125N* (Moreau et al., 2001). Unlike *mre11*Δ cells, very few differences were found between the *mre11-H125N* and wild-type cells (Figure 2A, S2A, S2H, S2I, Table S3 and Table S4). This absence of transcriptional differences was confirmed by RT-qPCR for a subset of pervasive non-coding transcripts in two different nuclease dead mutants (Figure S2C). At DNA breaks, MRX recruits the Tel1/ATM kinase through its interaction with Xrs2 (Nakada et al., 2003). To assess the involvement of Tel1 signaling in lncRNA transcriptional control, we measured by RT-qPCR the level of pervasive ncRNA in *tel1*Δ and *xrs2-11* mutants, which abrogate MRX-Tel1 interaction. Neither the absence of Tel1 nor the lack of interaction between MRX and Tel1 led to lncRNA accumulation (Figure S3A). Then, to rule out the possibility that the increased level of lncRNA observed in the absence of MRX is a general feature of DNA repair mutants, we also analyzed the transcriptome of *ku70*Δ mutants. In these cells, no transcriptional upregulation were detected by RNA-seq (Figure S3B). Finally, to exclude the possibility that pervasive transcription results from the persistence of unrepaired DNA lesions in the absence of MRX, we analyze the transcriptome of wild-type cells exposed to the DNA damaging agent MMS. As expected, MMS induced dramatic changes in the transcriptome profile (Figure S3B–E) (Travesa et al., 2012). Unlike the accumulation of transcripts observed in *rad50*Δ and *mre11*Δ cells, however, these changes included both increased and decreased expression of various transcripts (Figure S3C, S3D, Table S3 and Table S4). We conclude that the accumulation of mRNA and lncRNAs in the absence of MRX is neither due to loss of Mre11 nuclease activity,

nor to the signaling or recruitment of Tel1. It therefore differs from the transcriptional changes associated with DNA damage.

MRX represses transcription near its binding sites

As shown above, MRX mostly associates with the Cluster 1 subset of ORFs that also have high levels of the Mediator complex subunit Med17 and the RNAPII subunit Rpb1, suggesting that it might control gene expression close to its binding sites. To investigate this possibility, we quantified the expression of mRNAs and divergent ncRNAs transcribed from Cluster 1 ORFs in *rad50Δ* cells relative to wild-type cells; as a negative control, we did the same analysis for Cluster 2 ORFs, with which MRX and Mediator do not associate. Upregulation of expression of divergent ncRNAs in *rad50Δ* cells, when compared to wild-type cells, was significantly higher at Cluster 1 ORFs than it was at Cluster 2 ORFs (**Figure 2E**). Strikingly, this was not the case for mRNAs, which were overexpressed at similar levels from both Cluster 1 and Cluster 2 ORFs (**Figure 2F**). A similar analysis in mutants in which lncRNAs are stabilized (*rrp6Δ*, *xrn1Δ*; **Figure S3F**) showed no significant difference between expression of divergent ncRNAs from the two clusters (**Figure S3F**). Moreover, wild-type cells treated with MMS (WT+MMS) and *ku70Δ* mutants showed no overexpression bias for the Mediator-MRX-enriched cluster 1 (**Figure S3G**). Together, these data indicate that the MRX complex limits divergent ncRNA transcription across the genome, especially near its binding sites.

MRX is required to anchor the *GAL1-GAL10* locus to the NPC

Previous studies have found that tethering Mre11 to the *HMR* locus is sufficient to relocate this locus to the nuclear periphery and silence its expression (Kirkland and Kamakaka, 2013) and also that localization of *HMR* at the nuclear periphery requires the nucleoporin Nup60

(Ruben et al., 2011). Thus, we reasoned that the MRX complex might anchor other loci to NPCs. To test this hypothesis, we used the *GAL1-GAL10* locus, which relocates to the NPC when its transcription is induced by galactose (Drubin et al., 2006; Luthra et al., 2007). When the *GAL1-GAL10* locus was repressed by glucose, by ChIP-seq we found no Rad50 (MRX), Med17 (Mediator) or Rpb1 (RNAPII) enrichment at the site (Figure 3A). Upon transcriptional activation of the locus with galactose, by contrast, we saw robust recruitment of Rad50 to *GAL1-GAL10* genes body and terminators (Figure 3B, 90' galactose). Returning the cells to glucose disrupted the interaction between *GAL1-GAL10* and Rad50 (Figure 3B, 2h glucose). To see whether the *GAL1-GAL10* locus can relocate to the NPC in *rad50Δ* cells, we used a LacO/LacI-GFP tagging system in cells expressing a GFP-tagged Nup49 which allow to track a given locus position in the nucleus by fluorescent microscopy (Figure S4A; (Heun et al., 2001; Taddei et al., 2006b; Texari et al., 2013). In wild-type cells grown in glucose, the *GAL1-GAL10* locus is located mostly in the interior of the nucleus whereas when the cells are grown in raffinose (a non-repressive sugar) it is located more at the nuclear periphery; adding galactose to the cells for 90 minutes results in a yet larger proportion of the loci at the nuclear periphery (Figure S4B and see (Green et al., 2012). Upon 2 hours of glucose-induced repression, the locus gets back in the interior of the nucleus (Figure 3C). In *rad50Δ* cells, by contrast, the *GAL1-GAL10* locus did not relocate to the nuclear periphery when galactose was added for 90 minutes (Figure 3C). We note that the *GAL1-GAL10* locus is already less peripheral in non-repressive condition (raffinose) in *rad50Δ* in comparison to wild-type cells (32.1% vs 50.6% respectively, Figure 3C and Figure S4B). In fact, the absence of a functional MRX complex induces a nearly random nuclear position of the *GAL1-GAL10* regardless of the sugar/transcriptional status (Figure 3C) and delays *GAL10* mRNA accumulation (Figure S4C). In this respect, *rad50Δ* cells resembled *mlp1Δ mlp2Δ* nuclear pore mutants (Figure 3C and

S4C). Failure to relocate the *GAL1-GAL10* locus at the nuclear periphery in *rad50* Δ cells was confirmed using ChIP-qPCR on two independent PK-tagged subunits of the nuclear pore complex, namely Nic96 and Nup84 (**Figure 3D**). Like the transcriptional function of MRX, this Rad50-dependent relocation does not depend on the nuclease activity of the complex since relocation of the *GAL1-GAL10* locus to the nuclear periphery also occurs in an *mre11-H125N* mutant (**Figure 3C**). However, *GAL1-GAL10* relocation to the nuclear periphery was abolished in a *rad50-K40A* allele, which is devoid of ATPase activity (**Figure S4B**). Lastly, we found that *GAL1-GAL10* relocalization at the nuclear periphery neither involved Tel1/ATM signaling nor its recruitment by the MRX complex as both *tel1* Δ mutant and the *xrs2-11* allele were proficient to relocate the *GAL1-GAL10* locus to the nuclear periphery (**Figure S4D and S4E**). These results suggest that the MRX complex is required to relocate the *GAL1-GAL10* locus from the nuclear interior to the NPC, independently of Mre11 and Tel1/ATM activities.

Global chromatin-NPC interactions relies on the MRX complex

Since Rad50 is necessary to target the *GAL1-GAL10* locus to the NPC, we investigated whether the MRX complex might be required in general for chromatin interactions with the NPC. To do so, we first compared MRX binding sites with sites of contacts with the NPC genome-wide. Thus, we generated a map of NPC–chromatin interactions in G₁-phase cells by using Mlp1 ChIP–seq, as previously described (Casolari et al., 2004, 2005). This genome-wide map showed that Rad50 and Mlp1 associate with similar regions of chromatin in G₁-phase cells, as shown, for example, on a region of chromosome IV (**Figure S4F**). To characterize further this association, we compared the genome-wide distribution of Mlp1 and Rad50 by using heatmaps and metagene analysis centered on the TSSs and the TTSs of annotated ORFs sorted and divided into Cluster 1 and Cluster 2 (**Figure 4A**), as defined above. This analysis found Mlp1

preferentially associated with ORFs in Cluster 1, which are enriched in Rad50 and Med17, but it was also found at a relatively large number of ORFs in the Rad50–Med17-poor Cluster 2 (**Figure 4A** and **4B**). Mlp1 bound to promoters and gene bodies whereas Rad50 was mostly found in intergenic regions (**Figure 4A**). Measuring the ChIP-seq enrichment of Mlp1 at Rad50 peaks shows that MRX-bound DNA regions are contacting the NPC (**Figure S4G**). Thus, we wondered whether these two complexes might interact physically. To address this possibility, we used a strain that expresses an HA-tagged Nup60 (a NPC protein) and a Myc-tagged Xrs2 (a MRX component). Immunoprecipitation of Nup60-HA co-immunoprecipitated Xrs2-Myc (**Figure 4C**). Together, these data indicate that the NPC and MRX complexes interact physically and that highly transcribed genes enriched in Mediator and MRX are contacting the NPC.

Because the MRX complex is required to anchor the *GAL1-GAL10* locus to the nuclear periphery, interacts physically with the NPC and overlaps with Mlp1 on chromatin, we reasoned that MRX might play a role in chromatin anchoring to the NPC at MRX-binding sites. To test this possibility, we first performed single-locus tracking by microscopy using LacO/LacI-GFP tagging system in cells expressing a fluorescently-tagged nuclear periphery. These loci include the constitutively expressed ribosomal protein gene *RPL9A* and three mating pheromone inducible genes (*FIG2*, *PRM1* and *FUS3*). In wild-type cells, *RPL9A* colocalized with the nuclear periphery in ~ 60% of the cells and addition of mating pheromone induced repositioning of *FIG2*, *PRM1* and *FUS3* from the nuclear interior to the periphery (**Figure 4D**). Loss of Rad50 blocked *FIG2*, *PRM1* and *FUS3* relocalization to the nuclear periphery in the presence of mating pheromone and decreased significantly the constitutive peripheral localization of *RPL9A* (**Figure 4D**). To extend our observations genome-wide, we next performed ChIP-seq using an antibody against Mlp1-GFP as an assay for chromatin–NPC interactions. We calculated the average Mlp1 signal intensity from all Mlp1-enriched loci in

wild-type yeast and in a *rad50Δ* strain. The metagene analysis revealed that Mlp1 binding to chromatin was substantially reduced in cells lacking a functional MRX complex (**Figure 4E** and **4F**). Failure to anchor chromatin at the NPC in *rad50Δ* cells was confirmed by ChIP-qPCR for a subset of loci using an antibody against Nic96-PK, another NPC subunit (**Figure S4H**). The Mlp1 signal intensity in *rad50Δ* cells was significantly higher than in the signal obtained with the same antibody in a strain lacking a GFP epitope (unspecific control), however, indicating that a fraction of Mlp1 still bound to chromatin in the absence of Rad50 (**Figure 4E** and **4F**). This suggests that other mechanisms may also target chromatin to the NPC. To assess the involvement of MRX in the association of Mlp1 with chromatin, we sorted the Mlp1-enriched loci into five equal bins that differed in the amount of Rad50 associated with them (**Figure 4G**). In wild-type cells, Mlp1 enrichment was strictly proportional to Rad50 levels (**Figure 4G**). Consistent with this, Mlp1 loss from chromatin in *rad50Δ* cells when compared to wild-type cells was exacerbated at loci with the highest level of Rad50 (**Figure 4G** and **Figure S4I**). Thus, we conclude that MRX is required to tether chromatin to the NPC, especially the chromatin near MRX-binding sites.

The interaction between genes and NPCs is not essential for their transcription but, rather, helps to fine-tune inducible gene expression ([Green et al., 2012](#); [Rohner et al., 2013](#); [Taddei, 2007](#); [Texari et al., 2013](#)). As shown above, the lack of MRX reduced chromatin–NPC interactions and led to the accumulation of numerous pervasive transcripts. To assess whether NPC tethering is important for repression of pervasive non-coding transcription, we measured the levels of lncRNAs in the *mlp1Δ mlp2Δ* NPC mutant, which failed to anchor chromatin. Consistent with the MRX mutants ncRNA accumulation phenotype, *mlp1Δ mlp2Δ* cells had higher and similar to *rad50Δ* cells steady-state levels of sense (CUT882 and CUT669) and antisense ncRNAs (as-PHO11), as determined by RT-qPCR, than had wild-type cells (**Figure**

4H). These data indicate that NPC–MRX-mediated anchoring of chromatin correlates with an optimal repression of pervasive non-coding transcription.

MRX promotes the establishment of chromosomal domains

In yeast, promoters highly enriched in Mediator form strong boundaries between CIDs (Chereji et al., 2017; Hsieh et al., 2015) and we show above that MRX colocalizes with Mediator at promoter regions of genes that interact with the NPC. Thus, we wondered whether MRX might also be enriched at CID boundaries. To investigate this possibility, we created a MicroC-XL chromosome folding map of the genome of wild-type yeast, from which we could identify CIDs (Hsieh et al., 2016). We sorted the CID boundaries according to their insulation strength (i.e. ability to block adjacent CID interactions) and plotted the enrichment of the MRX protein Rad50, as well as the Med17 subunit of Mediator, the NPC protein Mlp1 and a subunit of the RSC remodeler, Sth1, according to ChIP–seq data (**Figure 5A**). This analysis found that Rad50 was enriched at a subset of strong CID boundaries that also contains Med17 and Mlp1 (**Figure 5A**), consistent with colocalization of Mlp1 with the MRX complex. This indicates that Mediator, MRX and Mlp1 associate at boundaries in a strength-dependent manner. By contrast, Sth1 was found associated with all the CID boundaries identified (n= 1790; **Figure 5A**). To compare the relative insulation strengths of the boundaries enriched in Rad50, Med17 and Mlp1, with those that were not enriched in these proteins, we assigned each boundary to the closest ORF in Cluster 1 or Cluster 2, as defined above (**Figure S5A**). CID boundaries enriched in Med17, Rad50 and Mlp1 in Cluster 1 had more robust boundary activity than those in Cluster 2 (**Figure 5B**). This suggests that NPC–chromatin interactions may contribute to CID boundary insulation. If so, the insulation strength of boundaries should diminish in the absence of the MRX-mediated NPC–boundary interaction. To test this prediction, we

generated Micro-C XL chromosome folding maps for paired *rad50Δ* and wild-type cells and found that Med17–Rad50-enriched boundaries (Cluster 1) were weaker in *rad50Δ* cells than in wild-type, whereas there was no effect of *rad50Δ* on the insulation score of Med17–Rad50-poor boundaries (Cluster 2; **Figure 5C**). To verify this role of the MRX complex in boundary insulation strength, we first grouped CID boundaries into five equal bins each with different amounts of Rad50 (**Figure S5B**). In wild-type cells, we found the highest insulation score for boundaries with the most Rad50 (Bin 1; **Figure S5B**). Consistent with this, the presence of MRX promotes significant boundary activity only at boundaries associated with the highest level of Rad50 (**Figure 5D and Figure S5C**). Lastly, we checked if loss of CID boundaries activity had an impact on local transcription directionality by comparing the increase in divergent ncRNA level by RNA-seq in *rad50Δ*/WT cells relative to the reduction of CID boundaries insulation strength by MicroC-XL in *rad50Δ*/WT. This analysis did not reveal an obvious correlation between CID boundaries weakening and a loss of transcriptional directionality (**Figure S5D**). Separating CID boundaries in highly (n=180, 10%) and weakly (n=1611, 90%) Rad50-dependent for insulation strength revealed a similar and non-significant increase of divergent ncRNA accumulation when CID boundaries strength is weakened or not (**Figure S5E and F**). Thus, we conclude that weakening CID boundaries does not locally affect transcription directionality. Overall, our results indicate that MRX and Mlp1 associate with CID boundaries in yeast, and that the loss of MRX integrity decreases CID insulation. This supports our hypothesis that in the absence of MRX, chromatin architecture is less constrained genome-wide.

Discussion (1365 words)

Using *S. cerevisiae*, we demonstrate a novel role for MRX in transcription control that is distinct from its role in DNA-damage and dependent upon the structural features of the complex, promoting chromatin-NPC interactions. We find that MRX is implicated in the establishment and/or maintenance of chromosomal domains, which repress a subset of non-coding and coding transcripts. Our work sheds light on a new function for the MRX complex and improves our understanding of how chromatin anchoring to the nuclear periphery can contribute to the accurate control of genome expression. The model in Figure 6 depicts the MRX complex recruited to highly transcribed gene promoters which also are strong CID boundaries. Through its interaction with the NPC protein Nup60, MRX contributes to the localization of certain loci to the nuclear periphery. This chromatin anchoring to the NPC may reinforce boundary activity which limits contacts between adjacent CIDs. The presence of the MRX complex favors directional initiation of transcription at promoters and limits the accumulation of unstable lncRNAs.

We report here that MRX limits the accumulation of numerous non-coding RNAs expressed from yeast promoters. This repressive function apparently contrasts with previous studies in which MRX and MRN have been implicated in transcription activation. For example, yeast *mre11* mutants fail to express properly a set of meiotic genes during sporulation (Kugou et al., 2007). In human cells, MRN promotes the expression of an androgen-induced transcriptional program by allowing the activation of androgen receptors bound enhancers. Androgen-induced enhancers are activated by a topoisomerase I-induced DNA nick which releases torsional stress. In this context, MRN-dependent DNA repair is thought to maintain enhancers activity (Puc et al., 2015). Moreover, MRN can act as a platform to recruit the pre-initiation complex and the RNAPII machinery at DSBs, which results in local production of non-

coding RNAs that have been proposed to be required to complete the repair process (Michelini et al., 2017; Pessina et al., 2019). Although there is no doubt that MRX and MRN can stimulate transcription in specific contexts such as these, our study shows that the complex is dispensable for expression of the majority of genes in *S. cerevisiae* when cells are growing exponentially in rich medium. Instead, our data indicate that MRX limits the expression of a subset of noncoding and coding transcripts across the yeast genome.

Our study reveals a role for MRX in insulating CID from each other. MRX is present at the strongest CID boundaries, along with Mediator and chromatin remodelers. Moreover, the absence of MRX specifically weakens these boundaries leading to increased chromosomal contacts between adjacent CIDs. Consistent with this function, we found MRX upstream of the TSS and downstream of the TTS on genes that are highly enriched in Mediator and RNAPII in G₁ phase cells and these very active promoters are known from previous studies to define boundaries between CIDs (Chereji et al., 2017; Hsieh et al., 2015). Boundary establishment/maintenance require the presence of Mediator, the cohesin loader Scc2, the chromatin modifier Rpd3, and the chromatin remodeler RSC (Hsieh et al., 2015; Rawal et al., 2018). Thus, our study adds the MRX complex to the list of factors implicated in the establishment/maintenance of many CID boundaries.

How MRX is recruited to intergenic regions of chromatin in G₁ remains unclear. The physical interaction between MRX and Mediator that we show here might contribute to MRX localization, but other factors may also be involved. One of these factors might be the RSC remodeler, which localizes to promoters during vegetative growth and is known to stabilize MRX at DNA breaks (Shim et al., 2007). The single-stranded DNA binding protein RPA, which binds to stalled replication forks and DSB (Seeber et al., 2016), may also be relevant for MRX recruitment to chromatin in the absence of replication or DNA damage since highly

transcribed genes were reported to be enriched in RPA (Sikorski et al., 2011). It is likely that several MRX recruitment mechanisms are involved in G₁ according to the local genomic context.

A key question is how MRX is able to repress non-coding transcription in yeast. Pervasive transcription originates from promoters and intragenic regions in actively transcribed chromatin. Cells control expression of noncoding transcripts both at the level of transcription and RNA stability; chromatin remodelers and histone modifying enzymes, for example, have essential roles in repressing pervasive transcription at the initiation step (Bagchi and Iyer, 2016). Here, we propose that the absence of MRX perturbs chromosome folding and positioning in the nucleus, which leads to enhanced ncRNA production. It is likely that the lack of MRX will also affect lower-order chromatin architecture at the nucleosome level which is of paramount importance to repel RNAPII and keep pervasive transcription in check. Indeed, several factors contributing to CIDs boundaries in yeast such as Rpd3 and RSC are also chromatin modifiers and remodellers which have been described to limit antisense transcription (Churchman and Weissman, 2011b; Gill et al., 2020; Hsieh et al., 2015; Marquardt et al., 2014). The fact that transcription of ncRNAs was not affected when the nuclease activity of Mre11 was inactivated supports the idea that it is the structural activity of MRX that is required and the nuclease activity of MRX is dispensable for its repressive function. This and the lack of effect of DNA damage or inactivation of the DNA repair factor Ku70 on ncRNA production argues for a specific structural function of the MRX complex in ncRNA repression that is unrelated to its repair activity or to spontaneous DNA damage. In line with this model, we also demonstrate that ncRNA accumulation does not occur if the MRX complex is not able to interact with Tel1/ATM or in the absence of Tel1.

Our study documents an unanticipated role for MRX in targeting chromatin to the NPC. A physical interaction between MRX and the NPC basket subunit Nup60 might contribute in part to this targeting but there are probably several mechanisms. A previous study, for example, reported that Mediator is required for gene–NPC contacts through an interaction with the nuclear export protein TREX2 (Schneider et al., 2015). Although MRX disruption abrogated relocation to the NPC of the *GAL1-GAL10* galactose-inducible locus and the mating pheromone-inducible loci *FIG2*, *PRM1* and *FUS3*, it only reduced constitutive NPC–chromatin interactions. This is consistent with the existence of multiple MRX-independent mechanisms targeting chromatin to the NPC (Randise-Hinchliff et al., 2016). These mechanisms may target specific types of loci to the NPC. For example, MRX promotes anchoring to the NPC specifically of chromatin containing loci that are strongly enriched in Rad50.

Chromatin anchoring to the NPC appears to be crucial for preventing the accumulation of pervasive transcripts. Whereas in specific genomic contexts, such as subtelomeric regions, *HMR/HML* loci and ribosomal genes, chromatin anchoring to the NPC is associated with transcriptional silencing (Gozalo et al., 2019; Kirkland and Kamakaka, 2013; Van de Vosse et al., 2011), we show here that cells with deletions of the NPC genes *MLP1/2* have generally higher levels of ncRNAs than have wild-type cells. Moreover, a majority of pervasive transcripts emanate from strong promoters and it is well established that most genes associated with NPCs are active genes (Akhtar and Gasser, 2007). NPC binding is not required for transcriptional activation of these genes (Raices and D’Angelo, 2017), but rather the NPC is enriched in chromatin modifying and remodeling activities that favor optimal expression in response to environmental fluctuations. MRX-dependent anchoring of chromatin to the NPC unique environment may also act to repress pervasive transcription.

Our findings suggest that, in addition to regulating pervasive transcription, NPC–MRX–chromatin interactions participate in establishing or maintaining CIDs/TADs boundaries and, more globally, chromosome organization in the nucleus. We show that NPC-bound chromatin correlates with strong CID boundaries in yeast. This is consistent with several previous studies showing NPC–chromatin interactions associated with the boundary/insulator effect in yeast (Ishii et al., 2002) and flies (Kalverda et al., 2008); the fly NPC protein Nup98 interacts with the zinc-finger, DNA-binding protein CTCF, which organizes the genome in metazoan by delimiting TADs (Cubebñas-Potts et al., 2017; Pascual-Garcia et al., 2017; Ramírez et al., 2018), and binding sites for Nup93 on chromatin coincide with those for CTCF (Phillips and Corces, 2009). Moreover, another link between regulation of divergent transcription and TAD boundaries comes from a study proposing that CTCF binding to Cohesin upstream of the most active promoters restricts divergent transcription in human cells (Bornelöv et al., 2015) and another showing that mammalian TAD boundaries are enriched in Cohesin and their formation requires both Cohesin and Mediator (Phillips-Cremins et al., 2013). We show here that MRX inactivation in yeast enhances pervasive transcription and interferes with chromatin–NPC interactions. Many of these pervasive transcripts are divergent lncRNAs. Thus yeast MRX might be the functional equivalent of mammalian Cohesin in this context, working in association with Mediator to promote transcriptional directionality.

Limitations and open questions

Our study reveals that loci exhibiting boundary activity between chromosomal interaction domains (CIDs) very often coincide with NPC, MRX and Mediator binding sites. Although this correlation supports the view that NPC-chromatin tethering contributes to chromosome folding and to boundaries insulation strength, our data do not formally prove it. Our work

suggests that MRX helps organize the genome into chromosomal domains anchored to the NPC, independently of its DNA repair function. Addressing the functional and physiological consequences of this genome organization function would require separation-of-function mutants of MRX unable to interact with the NPC but fully proficient for DNA repair. Moreover, we have recently observed that the MRX complex can also modulate the structure chromatin at stalled replication forks, independently of Mre11 nuclease activity (Delamarre et al., 2019). It is therefore possible that MRX represses the expression of a subset of coding and non-coding transcripts not only by promoting CID insulation through its interaction with the NPC, but also by modulating the structure of chromatin locally. Further work is required to address this possibility and to determine whether this novel role of MRX/MRN is conserved in multicellular organisms.

Acknowledgements

We thank members of the Pasero laboratory and Carol Featherstone for comments on the manuscript. We thank Ismaël Padioleau and Marc Describes for help with bioinformatics. We thank Jason Brickner, Elisa Dultz, Karsten Weis, Katsunori Sugimoto, Vincent Géli and Marie-Noëlle Simon for providing strains. We thank the Montpellier Ressources Imagerie (MRI) imaging facility. RF was supported by the University of Montpellier and RF and JP were supported by the *Association pour la Recherche contre le Cancer* (ARC). Work in the Pasero laboratory is supported by grants from the *Agence Nationale pour la Recherche* (ANR), *Institut National du Cancer* (INCa), the *Ligue Nationale Contre le Cancer (équipe labélisée)*, the *Fondation MSDAvenir* and by ARC and ANR (NIRO) grants to AL. This work has benefited from the facilities and expertise of the NGS platform of Institut Curie, supported by ANR grants ANR-10-EQPX-03 and ANR10-INBS-09-08 (investissements d'avenir) and by the Canceropôle Ile-de-France. Work in the Morillon lab was supported by the ANR (ANR-15-CE12-0007) and the ERC ("EpincRNA" starting grant & "DARK" consolidator grant).

Author contributions

JP, AL, PP, AM, MW, SMG, JS, OR, JC and KD designed the experiments. JP, AB, AL, MTE, MBB, NK, CD, AS, and KB performed the experiments. MS and KG did the libraries and sequencing. RF, US and MR did the bioinformatics. Supervision and Project administration: JP and AL. JP wrote the original draft. Writing, review, and editing: JP, AL, SMG, and PP.

Declaration of interests

The authors declare no competing interests.

Figures legends

Figure 1: MRX interacts with Mediator and binds intergenes in vegetative growth (A) ChIP-seq browser plots on chromosome IV of Rad50 (blue), Med17 (green, Eyboulet et al., 2013) and Rpb1 (grey) in wild-type strain synchronized in G₁ (Rpb1 and Rad50) or asynchronous (Med17). Signals are expressed as a ratio of the corresponding protein over input DNA, and for Rad50 ChIP minus the IP signal obtained in an untagged strain. ORF are indicated in black. Peaks filtered out by MACS2 and loci prone to generate artifact (Teytelman, 2013) are indicated by asterisks. (B) Rad50-HA ChIP-qPCR in G₁ cells in the promoter region of: *FIG2*, *GIC2*, *NRD1*, *ADH1* and *FAR1* (negative control). Data are expressed as a fold enrichment over the untagged strain IP. SEM is indicated (2 biological replicates). (C) Venn diagram showing the overlap of Rad50 and Med17 peaks. (D) Heatmaps and average profiles of Med17, Rpb1 and Rad50 from -1 kb from TSS to +1Kb to TTS. ORF were sorted and separated in two clusters (C1=656 and C2=3894) based on the level of Med17 signal intensity. Data are expressed as a ratio of the corresponding protein over input DNA. (E) Violin plots of ChIP-seq signal (RPKM) in wild-type cells for Med17, Rpb1 and Rad50 or RNA-seq (mRNA) in each cluster. Median is indicated. *** P -value $< 10^{-3}$, by two-sided Mann-Whitney paired test. (F) co-IP to test the interaction between Mediator and MRX. See also Figure S1 and Tables S1-S2.

Figure 2: MRX limits coding and non-coding transcription. (A) Density plots of RNA-seq signals expressed as a log₂ fold-change ratio for *rad50Δ*, *mre11Δ* and *mre11-H125N* over wild-type (WT) cells for mRNA (grey, n= 5798), long non-coding RNA (lncRNA) including CUT, SUT and XUT (red, n=3570) and divergent transcripts (green, n=5796). (B) Snapshot of lncRNA (red arrows) for WT, *rad50Δ*, and *mre11Δ* strains. The RNA-seq signals are visualized as a strand-

specific heatmap. The log₂ density turns from yellow to blue as the RNA-seq signal increases. (C) Scatter plot of RNA-seq tag density (log₂) for mRNA (n=5639), lncRNA (n=3374) and divergent ncRNA (n=5213) in WT versus *rad50Δ* cells. Transcripts differentially expressed are circled in colors, unchanged transcripts are colored in grey. (D) Pie charts illustrate the proportion of transcripts differentially expressed in *rad50Δ* versus WT. (E-F) Violin plots showing the transcription fold-change (*rad50Δ*/WT) in Med17-Rad50-enriched (cluster 1) versus Med17-Rad50-poor (cluster 2) regions for divergent ncRNA (E) and mRNA (F). *** *P*-value < 10⁻³, by two-sided Mann-Whitney paired test ; ns, not significant. See also Figures S2-3 and Tables S3-S4.

Figure 3: Relocation of *GAL1-GAL10* locus to the nuclear pore requires the MRX complex. (A) ChIP-seq browser plots on chromosome II of Rad50 (blue), Med17 (green, Eyboulet et al., 2013) and Rpb1 (grey) in wild-type strain grown in glucose medium, synchronized in G₁ (Rpb1 and Rad50) or asynchronous (Med17). Signals are expressed as a ratio of the corresponding protein over input DNA, and for Rad50 ChIP minus the IP signal obtained in an untagged strain. ORF are indicated in black. (B) Rad50 enrichment along the *GAL* locus was assessed by ChIP-qPCR in transcriptionally repressed (glucose), activable (raffinose) and induced (galactose) conditions. Data are expressed as a percentage of Input. SEM is indicated (4 biological replicates). Dash bars correspond to the IP value in an untagged strain. (C) Distribution of *GAL1-GAL10* locus in WT, *mlp1/2Δ*, *rad50Δ* and *mre11-H125N* strains when cells are grown in raffinose, galactose or glucose. * *P*-value < 10⁻³, by two-sided Fischer's Exact t-test; ns, not significant. (D) Nuclear pore subunits Nup84-PK or Nic96-PK ChIP-qPCR along the *GAL1-GAL10* locus. Data are expressed as a ratio of induced (galactose) over repressed (glucose) conditions. SEM is indicated (2 biological replicates). See also Figure S4.

Figure 4: Global chromatin-NPC interaction relies on the MRX complex. (A) Heatmaps and average profiles of Mlp1 and Rad50 from -1 kb from TSS to +1kb to TTS. ORF were sorted and separated in two clusters (C1=656 and C2=3894 ORF) as in Figure 1. Data are expressed as a ratio of the corresponding protein over input DNA. Rad50 heatmap is based on the same data presented in Figure 1D. (B) Violin plots of Mlp1 ChIP-seq signal (RPKM) in WT cells in each cluster. Median is indicated. *** P -value $< 10^{-3}$, by two-sided Mann-Whitney paired test. (C) co-IP to test the interaction between Nup60 and Xrs2. (D) Distribution of *FIG2*, *PRM1*, *FUS3* and *PRL9A* loci in WT and *rad50Δ* strains when cells are exponentially growing (async) or synchronized in G₁ (*FIG2*, *PRM1* and *FUS3*). * P -value $< 10^{-3}$, by two-sided Fischer's Exact paired t-test; ns, not significant. (E) Average profile of Mlp1 signal (ratio IP/input) ranging from -1 kb from TSS to +1Kb to TTS in WT and *rad50Δ* cells on ORFs exhibiting an enrichment for Mlp1 in a WT strain. Unspecific enrichment (IP in untagged strain) is shown for comparison purpose. (F and H) Violin plots representing Mlp1 ChIP-seq signal (RPKM) in WT cells in each cluster (F) or the ratio of Mlp1 ChIP-seq signals fold-change (*rad50Δ*/WT) in five bins (n=312) defined on Rad50 level at Mlp1-enriched loci (G). (F) Median is indicated. (G) Mean Rad50 (blue) and Mlp1 (purple) levels are indicated with histograms. *** P -value $< 10^{-3}$, by two-sided Mann-Whitney paired test; ns, not significant. (G). (H) RNA level determined by RT-qPCR from total RNA normalized over *ACT1*. See also Figure S4.

Figure 5: MRX promotes chromosomal interaction domains (CID) insulation. (A) Heatmaps of Sth1, Med17, Mlp1, and Rad50 from -10 kb to +10Kb of CID boundaries (n=1790). Boundaries were sorted according to their insulation strength defined in a WT strain. Data are expressed as a ratio of the corresponding protein over input DNA. (B-C) Violin plots

representing the MicroC-XL signals (contacts) between adjacent CIDs through a given boundary in either cluster (B) or the MicroC-XL signal fold-change (*rad50Δ*/WT) (C). Median is indicated. *** P -value $< 10^{-3}$, by two-sided Mann-Whitney paired test; ns, not significant. (D) Scatter plot representing MicroC-XL fold-change (*rad50Δ*/WT) and Rad50-HA ChIP-seq enrichment versus WT CID boundaries sorted by insulation strength. See also Figure S5.

Figure 6: MRX tethers chromatin at nuclear pores and limits genome expression. The MRX complex is recruited to highly transcribed gene promoters where it exhibits a boundary activity for adjacent chromosomal interaction domains (CID). Through an interaction with the nucleoporin Nup60, MRX positions nuclear pore complex (NPC)-interacting loci to the nuclear periphery. The presence of the MRX complex favors directional initiation of transcription (black arrows) at promoters and limits the accumulation of unstable lncRNA (red arrows). Chromatin anchoring to the NPC may reinforce boundary activity which limits contacts between adjacent CIDs. When MRX integrity is compromised, chromatin detaches from the NPC, boundaries insulation strength decreases, and adjacent CIDs exhibit more frequent contacts (grey arrows). Physical interactions are indicated with orange round arrows.

STAR METHODS

Resource availability

Lead contact

Further information and requests for resources and reagents should be directed to and will be fulfilled by the Lead Contact, Jérôme Poli (jerome.poli@igh.cnrs.fr).

Materials availability

All unique strains generated in this study are available from the Lead Contact without restriction. Requests for strains donated by other laboratories should be directed to the specific laboratory from which they were received. This study did not generate new unique reagents.

Data and code availability

Sequencing data generated in this study are deposited on Gene Expression Omnibus (<https://www.ncbi.nlm.nih.gov/geo/>) with the accession numbers: GSE148170; GSE136605 for γ -H2A) and on NCBI Sequence Read Archive (SRA) under the accession numbers SRP125409 (G₁ phase) and SRP189465 (G₁ + Zeocin (100ug/ml for 1h, S phase and S phase +200mM HU for 1h). RNA-seq data can be directly visualized on this website (<http://vm-gb.curie.fr/MRX/index.htm>). Raw images for Figure 1F, 4C and Supplemental Figure S1J are deposited on Mendelay data (<http://dx.doi.org/10.17632/3typz6j2hk.1>).

Experimental model and subject details

All *Saccharomyces cerevisiae* strains used are haploid and derived from W303 or JKM179 (see Table S5).

Method Details

Yeast strains and cultures

All strains used are listed in Table S5. YEP medium was supplemented with 2% glucose unless otherwise indicated. *MATa* cells were synchronized in G₁ by adding α -factor (5 $\mu\text{g}\cdot\text{ml}^{-1}$) for 170 min at 25°C.

Chromatin immunoprecipitation (ChIP)

ChIP was performed as described in (Delamarre et al., 2019) using anti-PK clone SV5-Pk1 (Serotec, MCA1360G), anti-RNAPII CTD 8WG16 (Abcam, ab817), anti-HA (Santa Cruz, SC-7392) and anti-GFP (ThermoFischer, A-11122) coupled to Dynabeads (Invitrogen, protein A and sheep anti-mouse M280 IgG). For quantitative PCR, background controls was determined using an untagged strain and enrichment was normalized to chromatin Input. Oligos used are listed in Table S6.

Genome wide profiling

ChIP sequencing libraries were prepared using ThruPLEX DNA-seq kit (Rubicon Genomics) Next generation sequencing was performed on a HiSeq4000 (Illumina). Single-end reads of 50 bp were aligned to *S. cerevisiae* genome (2011) sequence with Bowtie2, allowing only perfect matches. ChIP-seq profiles expressed as RPKM (Reads Per Kilobase per Million mapped reads) were obtained as a ratio of IP on Input reads. Profiles were generated with Deeptools2. Data are available on GEO (accession number GSE148170 and GSE136605 for γ -H2A).

RNA extraction, RT and RNA-seq

Total RNA was extracted from G₁ synchronized cells using standard hot phenol procedure. RT-qPCR were performed from three independent biological replicates, starting with 3ug of RNA. Strand-specific total RNA-seq libraries were prepared from rRNA-depleted total RNA preparation using biological duplicates of each strain with the TruSeq kit (Illumina) and sequenced by paired-end 2x50 bp. All bioinformatics analyses used uniquely mapped reads. Tags densities were normalized using the size factors from the R package DESeq2 (function `estimateSizeFactorsForMatrix()`, run on the whole count matrix). Data can be directly visualized on this website (<http://vm-gb.curie.fr/MRX/index.htm>).

Co-Immunoprecipitation (co-IP)

Coimmunoprecipitation experiments for Mediator-Rad50 interaction were performed as previously described (Eychenne et al., 2016). Whole cell extracts were prepared by disrupting HA-tagged yeast cells in lysis buffer (50 mM Tris-HCl [pH 7.5], 15% glycerol, 5mM MgCl₂ and antiprotease mix) in Mikro-Dismembrator S (Sartorius Stedim Biotech S.A.). After centrifugation at 13,000 × g for 20 min, the resulting supernatant plus 100 mM NaCl and Igepal 0.05% was used as input. Before immunoprecipitation, the extracts were pre-cleared by incubation with beads (Pan mouse IgG, Invitrogen) for 30 min at RT. HA-tagged proteins were immunoprecipitated using HA isolation kit (Miltenyi Biotec), following the manufacturer's instructions. All washes were performed using the lysis buffer. The 12CA5 anti-HA antibodies were used against HA-tagged proteins and the M2 anti-Flag antibody (Sigma) were used against Flag-tagged proteins.

Coimmunoprecipitation experiments for Nup60-Xrs2 interaction were performed as follow. Yeast cells were harvested in log phase. Cell pellets were resuspended in 0,6 ml of CoIP buffer (20 mM HEPES, 150 mM Kac, 2 mM MgCl₂, 10% glycerol, 0,01% Tween20, proteases inhibitor cocktail (Complete ULTRA SIGMA, 5892988001), phosphatase inhibitor (PhosStop SIGMA, 4906837001)). Cells were lysed using glass bead (Precellys lysing kit OZYME, 03961-1-0044) in Precellys system (3 times 45 secondes at 6500 rpm, with 1 minute ice break). Chromatin was sheared into 300bp fragments and centrifuged at 4°C at 13,000 rpm for 15 minutes. Supernatant was treated with 250 units of Benzonase endonuclease for 1mg proteins (SIGMA E1014-5KU) and incubated 1 hour at 4°C to digest DNA. Full digestion of DNA was checked by migration on a 1% agarose gel. Benzonase treated supernatant was incubated 1h at 4°C with 50 µl anti-HA magnetic beads (FISHER, 88837). Beads were washed three times with 1,5 ml of CoIP Buffer, and eluted with 20 µl of Laemmli buffer and subsequently subjected to SDS gel electrophoresis and transfer. Nup60-HA was detected anti-HA antibody (Abcam, ab9110) and Xrs2-Myc with anti-MYC antibody (Abcam, ab32).

Quantification of DSBs.

We quantified DSBs using qDSB-Seq method (Zhu et al., 2019) with NotI spike-in DSBs and i-BLESS DSB labeling. DSB sequencing data was analyzed using iSeq and qDSB-Seq software (<https://github.com/rowickalab/qDSB-Seq>) and custom scripts. The dataset generated for i-BLESS analysis are available on NCBI Sequence Read Archive (SRA) under the accession numbers SRP125409 (G₁ phase; (Biernacka et al., 2018)) and SRP189465 (G₁ + Zeocin (100ug/ml for 1h, S phase and S phase +200mM HU for 1h; (Zhu et al., 2019)) .

Microscopy and image analysis

Cells were fixed in fresh paraformaldehyde (PFA) 4% w/v for 1 min, washed 3 times in PBS and then attached to a #1.5H (0.17 mm) glass coverslip using Concanavalin A. They were imaged by taking 50 z slices of 200 nm thickness. Two microscopes were used to acquire images (Note: each replica series was done on the same day on the same microscope). For the majority of the replicates an Olympus IX70 microscope equipped with a Andor Zyla 4.2 Plus sCMOS camera, Marzhauser XY motorized stage, Prior Nano scan Z piezo, and a UPlan S APO 100x NA=1.4 oil objective was used due to the large field of view afforded by the sCMOS chip. GFP was excited using a Prior Scientific Lumen 200 Pro with a Semrock Brightline 485/20 filter and Pentaedge 4DB beamsplitter. Emission signals were captured through a 525/30 Semrock Brightline filter. In some instances, an Axioimager M1 microscope equipped with a Yokogawa CSU-X1 scanhead, Rolera Thunder Back illuminated EM-CCD (Q imaging), ASI MS-2000 Z piezo and a A plan-NEOFLUAR 100x NA=1.45 oil objective was used. GFP was excited with a Toptica iBeamSmart 488 laser with a Semrock Brightline Dio1 4DB dichroic filter. Emission signals were captured through a Chroma ET525/50nm filter. Fluorescence images were deconvolved using Huygens professional and the classic maximum likelihood estimate algorithm with a signal/noise ratio of 5, automatic background estimation and 40 iterations. Calculation of foci into nuclear zones was done as in (Horigome et al., 2014) for at least 200 cells/condition.

ChIP-seq peak calling

Rad50 and Med17 ChIP-seq peaks were determined using MACS2 software (Zhang et al., 2008) with the following options “*-gsize 9996000 -qvalue 10e-2 -mfold 500 -e100 -nomodel*” and the corresponding input sample as a control. Peaks in proximity ($d < 1\text{kb}$) were merged. This gave us a list of peaks significantly enriched for a given factor relative to the corresponding input DNA. For specificity control, we used MACS2 with the same parameters

to find peaks in an unspecific IP (untagged strain). Peaks found in the unspecific IP that were also detected in the specific IP were discarded. Additionally, we also discarded peaks overlapping with regions prone to generate ChIP artifacts described in Teytelman et al. 2013. For Med17, we only kept peaks identified in two independent Med17 IP from Eyboulet et al. 2013. Med17 & Rad50 peaks were intersected using *bedtools_intersectbed/2.27.1* from *samtools* (Quinlan and Hall, 2010) using the options “-v and a required overlap of 1bp”.

Creation of ORFs clusters based on the level of Med17-Rad50

ORFs were split in two clusters based on Med17 level using *computeMatrix* and *plotHeatmap* softwares from *Deeptools2* (Ramírez et al., 2016). First *computeMatrix* was used with the following input “Annotated_ORFs.bed (-R) and Med17 Bigwig (-S)” ; and the following options “-m 1000 -b 1000 -a 1000 -bs 50 --sortRegions descend --sortUsing mean --averageTypeBins mean --outFileSortedRegions”. Then *Matrix* was used to perform heatmap and clustering using *plotHeatmap* software from *Deeptools2* (Ramírez et al., 2016) using following options “-kmeans 2 -outFileSortedRegions --sortRegions descend”. This gave us a bed file: “ORFs_Med17_Sorted” containing all yeast ORFs sorted on Med17 level separated in two clusters (Med17-Rad50 enriched and Med17-Rad50 poor).

Heatmap & average profiles on ORF regions

Matrixes were generated using: *computeMatrix* with the following input “ORFs_Med17_Sorted.bed (-R)” and various Bigwigs (-S)” ; and the following options “-m 1000 -b 1000 -a 1000 -bs 50 --sortRegions keep --sortUsing mean --averageTypeBins mean --outFileSortedRegions”. Then *Matrix* was used to perform heatmap and clustering using

plotHeatmap software from Deeptools2 (Ramírez et al., 2016) using following options “--sortRegions keep --averageType mean”. Subsequent heatmaps were divided in two according to the number of genes in both clusters.

Average profiles were produced on each clusters. First, Matrixes were generated using computeMatrix with the following inputs “ORFs_Med17_Sorted_Cluster1.bed or ORFs_Med17_Sorted_Cluster1.bed (-R)” and various Bigwigs (-S) ; and the following options “-m 1000 -b 1000 -a 1000 -bs 50 --sortRegions keep --sortUsing mean --averageTypeBins mean --outFileSortedRegions”. Then, Matrix was used to perform average profiles using plotProfile software from Deeptools2 (Ramírez et al., 2016) using following options “--averageType mean”.

RPKM and violin plots on ORF regions (ChIP-seq)

RPKM on ChIP-seq were generated using bedtools MultiCovBed (Quinlan and Hall, 2010) with the following options “-f 1e-9 -r no -split no -q 0 -D no -F no -p no”. As Mediator and MRX localize in intergenic regions, we measured RPKM signals from -500nt of the ORF TSS to +500nt of the ORF TTS. Violin plots and statistical tests were made using R with a homemade script.

Script code is indicated below:

```
library("ggplot2", lib.loc=~R/win-library/3.5")
library(readr)
Input <- read_delim("Input.txt", "\t",
                   escape_double = FALSE, trim_ws = TRUE)
#view(Input)
#head(Input)
Input$ID <- as.factor(Input$ID)
#head(Input)
Violin <- ggplot(Input, aes(x=ID, y=Score)) +
  geom_violin(trim=FALSE)+
  geom_violin(trim=FALSE, fill='#A4A4A4', color="darkred")+
  geom_boxplot(width=0.1, fill="white")
```

```

VIOLIN_Input<-Violin + theme_classic() + scale_y_continuous(limits=c(according to input))
VIOLIN_Input
u_Input<-unstack(Input)
##head(u_Input)
wilcox.test(u_Input$CLUSTER1, u_Input$CLUSTER2)
median(u_Input$CLUSTER1)
median(u_Input$CLUSTER2)
ggsave("Input.emf", width = 11, height = 8)

```

Density and violin plots (RNA-seq)

Ratios were generated on RPKM. Density plots were made using R with a homemade script.

Script code is indicated below:

```

library(plotly)

p <- ggplot(Input, aes(Score, color = ID)) +
  scale_color_manual(values=c("#ED0000", "#677179", "#0131B4")) +
  geom_density(alpha = 1) +
  theme(panel.background = element_rect(fill = '#ffffff')) +
  xlim(c(-5, 5)) +
  ylim(c(0, 1.5))

```

p

RPKM were used to made violin plots using R with homemade following Script.

```

Violin <- ggplot(Input, aes(x=ind, y=values)) +
  geom_violin(trim=FALSE)+
  geom_violin(trim=FALSE, fill='#A4A4A4', color="darkred")+
  geom_boxplot(width=0.1, fill="white")+
  labs(title="Violin",x="Conditions", y = "Transcription")
Violin<-Violin + theme_classic() + scale_x_discrete(limits=c("x1", "x2")) +
scale_y_log10(limits=c(0.01,100000))

```

Identification of CID boundaries and insulation score with MicroC-XL

MicroC-XL was performed as previously described in Hsieh et al., 2016. MicroC-XL analyses were performed with Deeptools/Hicexplorer (Wolff et al., 2018). Fastq.gz were transformed with FASTQ Groomer (version 1.0.0). Mappings were done with BWA-MEM (Version 0.8.0) with the SacCer_Apr2011/sacCer3 as reference genome, with the following options “-p -k 19 -w 100 -r 1.5 -c 10000 -A 1 -B4 -O 6 -E 50 -L 0 -U 17 -T 30”. Matrixes were generated using:

hicBuildMatrix (Version 2.1.4.0) (Wolff et al., 2018) with the following options “-bs 100”. Then, Matrix was used to perform hicFindTADs (Wolff et al., 2018) with the following options “--minDepth 500 --maxDepth 5000 --step 100 --thresholdComparisons 0.01 --delta 0.001”. This allowed the identification of CID boundaries. To quantify CID boundaries strength, we generated RPKMs on MicroC-XL data using bedtools MultiCovBed (Quinlan and Hall, 2010) with the following options “-f 1e-9 -r no -split no -q 0 -D no -F no -p no”. This analysis gave a score for each CID boundary, which reflect the number of contacts through a given boundary that is proportional to its insulation potential. To assign CID boundaries in Med17-Rad50 ORFs clusters generated previously, and as CID boundaries are found in promoters, we determined the closest corresponding ORF.

Heatmap & average profiles around CID boundaries

For heatmaps around boundaries, matrixes were generated using: computeMatrix with the following input “Boundaries_Sorted_by_Strength or Boundaries_SortedBy_Med_Level (-R)” and various Bigwigs (-S) ; and the following options “-reference-point -b 10000 -a 10000 -bs 50 --sortRegions keep --sortUsing mean --averageTypeBins mean --outFileSortedRegions”. Then, Matrix was used to perform heatmap and clustering using plotHeatmap software from Deeptools2 (Ramírez et al., 2016) using following options “--sortRegions keep --averageType mean”.

RPKM and violin plots on CID boundaries (ChIP-seq)

RPKMs on ChIP-seq were generated using bedtools MultiCovBed (Quinlan and Hall, 2010) with the following options “-f 1e-9 -r no -split no -q 0 -D no -F no -p no”. Violin plots and statistical tests were made using R with a homemade Script. Script code is indicated below:

```
library("ggplot2", lib.loc=~ /R/win-library/3.5")
library(readr)
Input <- read_delim("Input.txt", "\t",
                    escape_double = FALSE, trim_ws = TRUE)
#view(Input)
#head(Input)
Input$ID <- as.factor(Input$ID)
#head(Input)
Violin <- ggplot(Input, aes(x=ID, y=Score)) +
  geom_violin(trim=FALSE)+
  geom_violin(trim=FALSE, fill='#A4A4A4', color="darkred")+
  geom_boxplot(width=0.1, fill="white")
VIOLIN_Input<-Violin + theme_classic() + scale_y_continuous(limits=c(according to
input))
VIOLIN_Input
u_Input<-unstack(Input)
##head(u_Input)
wilcox.test(u_Input$CLUSTER1, u_Input$CLUSTER2)
median(u_Input$CLUSTER1)
median(u_Input$CLUSTER2)
ggsave("Input.emf", width = 11, height = 8)
```

Creation of five ORFs and CID boundaries clusters based on Rad50 levels

RPKMs on Rad50 ChIP-seq were generated using bedtools MultiCovBed (Quinlan and Hall, 2010) with the following options “-f 1e-9 -r no -split no -q 0 -D no -F no -p no”.

ORFs or CID boundaries were sorted based on Rad50 levels and split in five clusters containing an equal number of genes.

Quantification and statistical analysis

All statistical tests and numbers of biological replicates are listed in the figure legends. Standard error of the mean (SEM) is indicated for ChIP-qPCR and RT-qPCR data. Distributions were compared using Mann-Whitney paired test (RNA-seq, ChIP-seq, MicroC-XL) and mean values were compared by two-sided Fischer's Exact t-test (Microscopy experiments).

Supplementary Tables

Note: Supplemental tables 1 to 4 are provided as Excel files.

Table S1. **MRX peaks coordinates (MACS2 peak calling), Related to Figure 1.**

Table S2. **MRX-Mediator enriched and poor clusters ORFs list and Gene Ontology, Related to Figure 1.**

Table S3. **Differentially expressed transcripts list (RNA-seq), Related to Figure 2.**

Table S4. **Differentially expressed transcripts Gene Ontology (RNA-seq), Related to Figure 2.**

Table S5. **Yeast strains used in this study. Related to STAR Method.**

Table S6. **Oligos used in this study. Related to STAR Method.**

References

- Ahmed, S., Brickner, D.G., Light, W.H., Cajigas, I., McDonough, M., Froysheter, A.B., Volpe, T., and Brickner, J.H. (2010). DNA zip codes control an ancient mechanism for gene targeting to the nuclear periphery. *Nat. Cell Biol.* *12*, 111–118.
- Akhtar, A., and Gasser, S.M. (2007). The nuclear envelope and transcriptional control. *Nat Rev Genet* *8*, 507–517.
- Bagchi, D.N., and Iyer, V.R. (2016). The Determinants of Directionality in Transcriptional Initiation. *Trends Genet.* *32*, 322–333.
- Biernacka, A., Zhu, Y., Skrzypczak, M., Forey, R., Pardo, B., Grzelak, M., Nde, J., Mitra, A., Kudlicki, A., Crosetto, N., et al. (2018). i-BLESS is an ultra-sensitive method for detection of DNA double-strand breaks. *Commun. Biol.* *1*, 181.
- Bornelöv, S., Komorowski, J., and Wadelius, C. (2015). Different distribution of histone modifications in genes with unidirectional and bidirectional transcription and a role of CTCF and cohesin in directing transcription. *BMC Genomics* *16*, 1–13.
- Cabal, G.G., Genovesio, A., Rodriguez-Navarro, S., Zimmer, C., Gadal, O., Lesne, A., Buc, H., Feuerbach-Fournier, F., Olivo-Marin, J.C., Hurt, E.C., et al. (2006). SAGA interacting factors confine sub-diffusion of transcribed genes to the nuclear envelope. *Nature* *441*, 770–773.
- Capelson, M., Liang, Y., Schulte, R., Mair, W., Wagner, U., and Hetzer, M.W. (2010). Chromatin-bound nuclear pore components regulate gene expression in higher eukaryotes. *Cell* *140*, 372–383.
- Casolari, J.M., Brown, C.R., Komili, S., West, J., Hieronymus, H., and Silver, P. a (2004). Genome-wide localization of the nuclear transport machinery couples transcriptional status

and nuclear organization. *Cell* *117*, 427–439.

Casolari, J.M., Brown, C.R., Drubin, D.A., Rando, O.J., and Silver, P.A. (2005). Developmentally induced changes in transcriptional program alter spatial organization across chromosomes. *Genes Dev.* *19*, 1188–1198.

Chereji, R. V., Bharatula, V., Elfving, N., Blomberg, J., Larsson, M., Morozov, A. V., Broach, J.R., and Björklund, S. (2017). Mediator binds to boundaries of chromosomal interaction domains and to proteins involved in DNA looping, RNA metabolism, chromatin remodeling, and actin assembly. *Nucleic Acids Res.* *45*, 8806–8821.

Churchman, L.S., and Weissman, J.S. (2011a). Nascent transcript sequencing visualizes transcription at nucleotide resolution. *Nature* *469*, 368–373.

Churchman, L.S., and Weissman, J.S. (2011b). Nascent transcript sequencing visualizes transcription at nucleotide resolution. *Nature* *469*, 368–373.

Cubeñas-Potts, C., Rowley, M.J., Lyu, X., Li, G., Lei, E.P., and Corces, V.G. (2017). Different enhancer classes in *Drosophila* bind distinct architectural proteins and mediate unique chromatin interactions and 3D architecture. *Nucleic Acids Res.* *45*, 1714–1730.

D’Amours, D., and Jackson, S.P. (2002). The Mre11 complex: at the crossroads of dna repair and checkpoint signalling. *Nat. Rev. Mol. Cell Biol.* *3*, 317–327.

Delamarre, A., Barthe, A., de la Roche saint André, C., Luciano, P., Forey, R., Padioleau, I., Skrzypczak, M., Ginalski, K., Géli, V., Lengronne, A., et al. (2019). Molecular Cell MRX increases chromatin accessibility at stalled replication forks to promote nascent DNA resection and cohesin loading. *Mol. Cell* 1–16.

Dieppo, G., Iglesias, N., and Stutz, F. (2006). Cotranscriptional Recruitment to the mRNA

Export Receptor Mex67p Contributes to Nuclear Pore Anchoring of Activated Genes. *Mol. Cell Biol.* *26*, 7858–7870.

van Dijk, E.L., Chen, C.L., d'Aubenton-Carafa, Y., Gourvennec, S., Kwapisz, M., Roche, V., Bertrand, C., Silvain, M., Legoix-Ne, P., Loeillet, S., et al. (2011). XUTs are a class of Xrn1-sensitive antisense regulatory non-coding RNA in yeast. *Nature* *475*, 114–117.

Drubin, D.A., Garakani, A.M., and Silver, P.A. (2006). Motion as a phenotype: The use of live-cell imaging and machine visual screening to characterize transcription-dependent chromosome dynamics. *BMC Cell Biol.* *7*, 1–12.

Dultz, E., Tjong, H., Weider, E., Herzog, M., Young, B., Brune, C., Müllner, D., Loewen, C., Alber, F., and Weis, K. (2016). Global reorganization of budding yeast chromosome conformation in different physiological conditions. *J. Cell Biol.* *212*, 321–334.

Eyboulet, F., Cibot, C., Eychenne, T., Neil, H., Alibert, O., Werner, M., and Soutourina, J. (2013). Mediator links transcription and DNA repair by facilitating Rad2/XPG recruitment. *Genes Dev.* *27*, 2549–2562.

Eyboulet, F., Wydau-Dematteis, S., Eychenne, T., Alibert, O., Neil, H., Boschiero, C., Nevers, M.C., Volland, H., Cornu, D., Redeker, V., et al. (2015). Mediator independently orchestrates multiple steps of preinitiation complex assembly in vivo. *Nucleic Acids Res.* *43*, 9214–9231.

Eychenne, T., Novikova, E., Barrault, M.-B., Alibert, O., Boschiero, C., Peixeiro, N., Cornu, D., Redeker, V., Kuras, L., Nicolas, P., et al. (2016). Functional interplay between Mediator and TFIIB in preinitiation complex assembly in relation to promoter architecture. *Genes Dev.* *30*, 2119–2132.

Eychenne, T., Werner, M., and Soutourina, J. (2017). Toward understanding of the

mechanisms of Mediator function in vivo: Focus on the preinitiation complex assembly. *Transcription* 8, 328–342.

Forey, R., Poveda, A., Sharma, S., Barthe, A., Padioleau, I., Renard, C., Lambert, R., Skrzypczak, M., Ginalska, K., Lengronne, A., et al. (2020). Mec1 Is Activated at the Onset of Normal S Phase by Low-dNTP Pools Impeding DNA Replication. *Mol. Cell*.

Fudenberg, G., Abdennur, N., Imakaev, M., Goloborodko, A., and Mirny, L.A. (2017). Emerging Evidence of Chromosome Folding by Loop Extrusion. *Cold Spring Harb. Symp. Quant. Biol.* 82, 45–55.

Gasser, S.M., and Laemmli, U.K. (1987). A glimpse at chromosomal order. *Trends Genet* 3, 16–22.

Gill, J.K., Maffioletti, A., García-Moliner, V., Stutz, F., and Soudet, J. (2020). Fine Chromatin-Driven Mechanism of Transcription Interference by Antisense Noncoding Transcription. *Cell Rep.* 31, 107612.

Gozalo, A., Duke, A., Lan, Y., Pascual-Garcia, P., Talamas, J.A., Nguyen, S.C., Shah, P.P., Jain, R., Joyce, E.F., and Capelson, M. (2019). Core Components of the Nuclear Pore Bind Distinct States of Chromatin and Contribute to Polycomb Repression. *Mol. Cell* 77, 1–15.

Green, E.M., Jiang, Y., Joyner, R., and Weis, K. (2012). A negative feedback loop at the nuclear periphery regulates GAL gene expression. *Mol. Biol. Cell* 23, 1367–1375.

Heun, P., Laroche, T., Raghuraman, M.K., and Gasser, S.M. (2001). The positioning and dynamics of origins of replication in the budding yeast nucleus. *J. Cell Biol.* 152, 385–400.

Hohl, M., Kwon, Y., Galvan, S.M., Xue, X., Tous, C., Aguilera, A., Sung, P., and Petrini, J.H.J. (2011). The Rad50 coiled-coil domain is indispensable for Mre11 complex functions. *Nat.*

Struct. Mol. Biol. *18*, 1124–1131.

Horigome, C., Oma, Y., Konishi, T., Schmid, R., Marcomini, I., Hauer, M.H., Dion, V., Harata, M., and Gasser, S.M. (2014). SWR1 and INO80 chromatin remodelers contribute to dna double-strand break perinuclear anchorage site choice. *Mol. Cell* *55*, 626–639.

Hsieh, T.H.S., Weiner, A., Lajoie, B., Dekker, J., Friedman, N., and Rando, O.J. (2015). Mapping Nucleosome Resolution Chromosome Folding in Yeast by Micro-C. *Cell* *162*, 108–119.

Hsieh, T.H.S., Fudenberg, G., Goloborodko, A., and Rando, O.J. (2016). Micro-C XL: Assaying chromosome conformation from the nucleosome to the entire genome. *Nat. Methods* *13*, 1009–1011.

Ishii, K., Arib, G., Lin, C., Van Houwe, G., and Laemmli, U.K. (2002). Chromatin boundaries in budding yeast: the nuclear pore connection. *Cell* *109*, 551–562.

Jani, D., Valkov, E., and Stewart, M. (2014). Structural basis for binding the TREX2 complex to nuclear pores, GAL1 localisation and mRNA export. *Nucleic Acids Res.* *42*, 6686–6697.

Jensen, T.H., Jacquier, A., and Libri, D. (2013). Dealing with pervasive transcription. *Mol. Cell* *52*, 473–484.

Kalverda, B., Röling, M.D., and Fornerod, M. (2008). Chromatin organization in relation to the nuclear periphery. *FEBS Lett.* *582*, 2017–2022.

Kirkland, J.G., and Kamakaka, R.T. (2013). Long-range heterochromatin association is mediated by silencing and double-strand DNA break repair proteins. *J. Cell Biol.* *201*, 809–826.

Kirkland, J.G., Peterson, M.R., Still, C.D., Brueggeman, L., Dhillon, N., and Kamakaka, R.T. (2015). Heterochromatin formation via recruitment of DNA repair proteins. *Mol. Biol. Cell* *26*, 1395–1410.

- Krietenstein, N., Wal, M., Watanabe, S., Park, B., Peterson, C.L., Pugh, B.F., and Korber, P. (2016). Genomic Nucleosome Organization Reconstituted with Pure Proteins. *Cell* 167, 709-721.e12.
- Kugou, K., Sasanuma, H., Matsumoto, K., Shirahige, K., and Ohta, K. (2007). Mre11 mediates gene regulation in yeast spore development. *Genes Genet. Syst.* 82, 21–33.
- Li, B., Carey, M., and Workman, J.L. (2007). The Role of Chromatin during Transcription. *Cell* 128, 707–719.
- Liang, Y., Franks, T.M., Marchetto, M.C., Gage, F.H., and Hetzer, M.W. (2013). Dynamic association of NUP98 with the human genome. *PLoS Genet.* 9, e1003308.
- Lisby, M., and Rothstein, R. (2004). DNA repair: keeping it together. *Curr Biol* 14, R994-6.
- Luthra, R., Kerr, S.C., Harreman, M.T., Apponi, L.H., Fasken, M.B., Ramineni, S., Chaurasia, S., Valentini, S.R., and Corbett, A.H. (2007). Actively transcribed GAL genes can be physically linked to the nuclear pore by the SAGA chromatin modifying complex. *J. Biol. Chem.* 282, 3042–3049.
- Marquardt, S., Escalante-Chong, R., Pho, N., Wang, J., Churchman, L.S., Springer, M., and Buratowski, S. (2014). A chromatin-based mechanism for limiting divergent noncoding transcription. *Cell* 157, 1712–1723.
- Michelini, F., Pitchiaya, S., Vitelli, V., Sharma, S., Gioia, U., Pessina, F., Cabrini, M., Wang, Y., Capozzo, I., Iannelli, F., et al. (2017). Damage-induced lncRNAs control the DNA damage response through interaction with DDRNAs at individual double-strand breaks. *Nat. Cell Biol.* 19, 1400–1411.
- Mimitou, E.P., and Symington, L.S. (2008). Sae2, Exo1 and Sgs1 collaborate in DNA double-

strand break processing. *Nature* 455, 770–774.

Moreau, S., Morgan, E.A., and Symington, L.S. (2001). Overlapping functions of the *Saccharomyces cerevisiae* Mre11, Exo1 and Rad27 nucleases in DNA metabolism. *Genetics* 159, 1423–1433.

Nakada, D., Matsumoto, K., and Sugimoto, K. (2003). ATM-related Tel1 associates with double-strand breaks through an Xrs2-dependent mechanism. *Genes Dev.* 17, 1957–1962.

Neil, H., Malabat, C., d'Aubenton-Carafa, Y., Xu, Z., Steinmetz, L.M., and Jacquier, A. (2009). Widespread bidirectional promoters are the major source of cryptic transcripts in yeast. *Nature* 457, 1038–1042.

Oh, J., and Symington, L.S. (2018). Role of the Mre11 complex in preserving genome integrity. *Genes (Basel)*. 9, 1–25.

Parnell, T.J., Schlichter, A., Wilson, B.G., and Cairns, B.R. (2015). The chromatin remodelers RSC and ISW1 display functional and chromatin-based promoter antagonism. *Elife* 2015, 1–21.

Pascual-Garcia, P., Debo, B., Aleman, J.R., Talamas, J.A., Lan, Y., Nguyen, N.H., Won, K.J., and Capelson, M. (2017). Metazoan Nuclear Pores Provide a Scaffold for Poised Genes and Mediate Induced Enhancer-Promoter Contacts. *Mol. Cell* 66, 63-76.e6.

Pessina, F., Giavazzi, F., Yin, Y., Gioia, U., Vitelli, V., Galbiati, A., Barozzi, S., Garre, M., Oldani, A., Flaus, A., et al. (2019). Functional transcription promoters at DNA double-strand breaks mediate RNA-driven phase separation of damage-response factors. *Nat. Cell Biol.* 21, 1286–1299.

Petty, E., and Pillus, L. (2013). Balancing chromatin remodeling and histone modifications in

transcription. *Trends Genet.* 29, 621–629.

Phillips-Cremins, J.E., Sauria, M.E.G., Sanyal, A., Gerasimova, T.I., Lajoie, B.R., Bell, J.S.K., Ong, C.T., Hookway, T.A., Guo, C., Sun, Y., et al. (2013). Architectural protein subclasses shape 3D organization of genomes during lineage commitment. *Cell* 153, 1281–1295.

Phillips, J.E., and Corces, V.G. (2009). CTCF: Master Weaver of the Genome. *Cell* 137, 1194–1211.

Puc, J., Kozbial, P., Li, W., Tan, Y., Liu, Z., Suter, T., Ohgi, K.A., Zhang, J., Aggarwal, A.K., and Rosenfeld, M.G. (2015). Ligand-dependent enhancer activation regulated by topoisomerase-I activity. *Cell* 160, 367–380.

Quinlan, A.R., and Hall, I.M. (2010). BEDTools: a flexible suite of utilities for comparing genomic features. *Bioinformatics* 26, 841–842.

Raices, M., and D’Angelo, M.A. (2017). Nuclear pore complexes and regulation of gene expression. *Curr. Opin. Cell Biol.* 46, 26–32.

Ramírez, F., Ryan, D.P., Grüning, B., Bhardwaj, V., Kilpert, F., Richter, A.S., Heyne, S., Dündar, F., and Manke, T. (2016). deepTools2: a next generation web server for deep-sequencing data analysis. *Nucleic Acids Res.* 44, W160-5.

Ramírez, F., Bhardwaj, V., Arrigoni, L., Lam, K.C., Grüning, B.A., Villaveces, J., Habermann, B., Akhtar, A., and Manke, T. (2018). High-resolution TADs reveal DNA sequences underlying genome organization in flies. *Nat. Commun.* 9, 189.

Randise-Hinchliff, C., Coukos, R., Sood, V., Sumner, M.C., Zdraljevic, S., Sholl, L.M., Brickner, D.G., Ahmed, S., Watchmaker, L., and Brickner, J.H. (2016). Strategies to regulate transcription factor-mediated gene positioning and interchromosomal clustering at the nuclear periphery.

J. Cell Biol. 212, 633–646.

Rawal, Y., Chereji, R. V., Qiu, H., Ananthkrishnan, S., Govind, C.K., Clark, D.J., and Hinnebusch, A.G. (2018). SWI/SNF and RSC cooperate to reposition and evict promoter nucleosomes at highly expressed genes in yeast. *Genes Dev.* 32, 695–710.

Rohner, S., Kalck, V., Wang, X., Ikegami, K., Lieb, J.D., Gasser, S.M., and Meister, P. (2013). Promoter- and RNA polymerase II-dependent hsp-16 gene association with nuclear pores in *Caenorhabditis elegans*. *J. Cell Biol.* 200, 589–604.

Ruben, G.J., Kirkland, J.G., MacDonough, T., Chen, M., Dubey, R.N., Gartenberg, M.R., and Kamakaka, R.T. (2011). Nucleoporin mediated nuclear positioning and silencing of HMR. *PLoS One* 6.

Schmid, M., Arib, G., Laemmli, C., Nishikawa, J., Durussel, T., and Laemmli, U.K. (2006). Nup-PI: the nucleopore-promoter interaction of genes in yeast. *Mol Cell* 21, 379–391.

Schneider, M., Hellerschmied, D., Schubert, T., Amlacher, S., Vinayachandran, V., Reja, R., Pugh, B.F., Clausen, T., and Köhler, A. (2015). The Nuclear Pore-Associated TREX-2 Complex Employs Mediator to Regulate Gene Expression. *Cell* 162, 1016–1028.

Seeber, A., Hegnauer, A.M., Hustedt, N., Deshpande, I., Poli, J., Eglinger, J., Pasero, P., Gut, H., Shinohara, M., Hopfner, K.P., et al. (2016). RPA Mediates Recruitment of MRX to Forks and Double-Strand Breaks to Hold Sister Chromatids Together. *Mol. Cell* 64, 951–966.

Seila, A.C., Core, L.J., Lis, J.T., and Sharp, P.A. (2009). Divergent transcription: a new feature of active promoters. *Cell Cycle* 8, 2557–2564.

Shim, E.Y., Hong, S.J., Oum, J.-H., Yanez, Y., Zhang, Y., and Lee, S.E. (2007). RSC Mobilizes Nucleosomes To Improve Accessibility of Repair Machinery to the Damaged Chromatin. *Mol.*

Cell. Biol. 27, 1602–1613.

Shroff, R., Arbel-Eden, A., Pilch, D., Ira, G., Bonner, W.M., Petrini, J.H., Haber, J.E., and Lichten, M. (2004). Distribution and Dynamics of Chromatin Modification Induced by a Defined DNA Double-Strand Break. *Curr. Biol.* 14, 1703–1711.

Sikorski, T.W., Ficarro, S.B., Holik, J., Kim, T.S., Rando, O.J., Marto, J.A., and Buratowski, S. (2011). Sub1 and RPA associate with RNA polymerase II at different stages of transcription. *Mol. Cell* 44, 397–409.

Soutourina, J. (2018). Transcription regulation by the Mediator complex. *Nat. Rev. Mol. Cell Biol.* 19, 262–274.

Stracker, T.H., and Petrini, J.H.J. (2011). The MRE11 complex: Starting from the ends. *Nat. Rev. Mol. Cell Biol.* 12, 90–103.

Szabo, Q., Bantignies, F., and Cavalli, G. (2019). Principles of genome folding into topologically associating domains. *Sci. Adv.* 5.

Taddei, A. (2007). Active genes at the nuclear pore complex. *Curr. Opin. Cell Biol.* 19, 305–310.

Taddei, A., Van Houwe, G., Hediger, F., Kalck, V., Cubizolles, F., Schober, H., and Gasser, S.M. (2006a). Nuclear pore association confers optimal expression levels for an inducible yeast gene. *Nature* 441, 774–778.

Taddei, A., Van Houwe, G., Hediger, F., Kalck, V., Cubizolles, F., Schober, H., and Gasser, S.M. (2006b). Nuclear pore association confers optimal expression levels for an inducible yeast gene. *Nature* 441, 774–778.

Texari, L., Dieppo, G., Vinciguerra, P., Contreras, M.P., Groner, A., Letourneau, A., and Stutz, F. (2013). The Nuclear Pore Regulates GAL1 Gene Transcription by Controlling the Localization

of the SUMO Protease Ulp1. *Mol. Cell* 51, 807–818.

Teytelman, L., Thurtle, D.M., Rine, J., and van Oudenaarden, A. (2013). Highly expressed loci are vulnerable to misleading CHIP localization of multiple unrelated proteins. *Proc. Natl. Acad. Sci. U. S. A.* 110, 18602–18607.

Tisseur, M., Kwapisz, M., and Morillon, A. (2011). Pervasive transcription - Lessons from yeast. *Biochimie* 93, 1889–1896.

Tittel-Elmer, M., Alabert, C., Pasero, P., and Cobb, J.A. (2009). The MRX complex stabilizes the replisome independently of the S phase checkpoint during replication stress. *Embo J* 28, 1142–1156.

Tittel-Elmer, M., Lengronne, A., Davidson, M.B., Bacal, J., François, P., Hohl, M., Petrini, J.H.J., Pasero, P., and Cobb, J.A. (2012). Cohesin Association to Replication Sites Depends on Rad50 and Promotes Fork Restart. *Mol. Cell* 48, 98–108.

Travesa, A., Kuo, D., De Bruin, R.A.M., Kalashnikova, T.I., Guaderrama, M., Thai, K., Aslanian, A., Smolka, M.B., Yates, J.R., Ideker, T., et al. (2012). DNA replication stress differentially regulates G1/S genes via Rad53-dependent inactivation of Nrm1. *EMBO J.* 31, 1811–1822.

Uhlmann, F. (2016). SMC complexes: From DNA to chromosomes. *Nat. Rev. Mol. Cell Biol.* 17, 399–412.

Van de Vosse, D.W., Wan, Y., Wozniak, R.W., and Aitchison, J.D. (2011). Role of the nuclear envelope in genome organization and gene expression. *Wiley Interdiscip. Rev. Syst. Biol. Med.* 3, 147–166.

Wery, M., Descrimes, M., Vogt, N., Dallongeville, A.S., Gautheret, D., and Morillon, A. (2016). Nonsense-Mediated Decay Restricts LncRNA Levels in Yeast Unless Blocked by Double-

Stranded RNA Structure. *Mol. Cell* *61*, 379–392.

Wolff, J., Bhardwaj, V., Nothjunge, S., Richard, G., Renschler, G., Gilsbach, R., Manke, T., Backofen, R., Ramirez, F., and Gruning, B.A. (2018). Galaxy HiCExplorer: a web server for reproducible Hi-C data analysis, quality control and visualization. *Nucleic Acids Res.* *46*, W11–W16.

Xu, Z., Wei, W., Gagneur, J., Perocchi, F., Clauder-Munster, S., Camblong, J., Guffanti, E., Stutz, F., Huber, W., and Steinmetz, L.M. (2009). Bidirectional promoters generate pervasive transcription in yeast. *Nature* *457*, 1033–1037.

Zhang, Y., Liu, T., Meyer, C.A., Eeckhoute, J., Johnson, D.S., Bernstein, B.E., Nusbaum, C., Myers, R.M., Brown, M., Li, W., et al. (2008). Model-based analysis of ChIP-Seq (MACS). *Genome Biol.* *9*, R137.

Zhu, Y., Biernacka, A., Pardo, B., Dojer, N., Forey, R., Skrzypczak, M., Fongang, B., Nde, J., Yousefi, R., Pasero, P., et al. (2019). qDSB-Seq is a general method for genome-wide quantification of DNA double-strand breaks using sequencing. *Nat. Commun.* *10*, 2313.

KEY RESSOURCE TABLE

REAGENT or RESOURCE	SOURCE	IDENTIFIER
Antibodies		
Anti-PK (anti-V5 tag)	AbD Serotec	Cat#MCA1360G; RRID: AB_1172162
Anti-HA	Santa Cruz	Cat#SC-7392; RRID: AB_627809
Anti-HA (12CA5)	Roche	Cat# 11 666 606 001
Anti-HA	Abcam	Cat#Ab9110
Anti-MYC	Abcam	Cat#Ab32
Anti-FLAG M2	Sigma	Cat#B3111
Anti-GFP	ThermoFischer	Cat#A-11122
Anti-Rpb1-CTD (clone 8WG16)	Abcam	Cat#AB817
ECL anti-mouse IgG from sheep	Life Technologies	Cat#NA931RRID: AB_627809 ;
Chemicals, Peptides, and Recombinant Proteins		
BSA	Biorad	Cat#500-0207
Glass beads	Yasui Kikai, Osaka	Cat#MB400U
Proteinase K	Sigma	Cat#P6556
RNase A DNase-free	Sigma	Cat#R6513
Glucose	VWR	Cat#R101175P
Galactose	Sigma	Cat#G0750
HEPES-KOH	Sigma	Cat#H3375-500G
Dynabeads protein A	Life Technologies	Cat#100.02D
IGEPAL	IGEPAL	Cat#I3021
Glycogen	Roche	Cat#10901393001
Glycine	Sigma	Cat#G8898
Formaldehyde	Sigma	Cat#F8775
NaCl	Sigma	Cat#S3014
cOmplete tablet	Roche	Cat#5056489001
Pronase 50K	VWR	Cat#53702-50
α -factor	Biotem	alpha-factor
Na-deoxycholate	Sigma	Na-deoxycholate
Phenol:Chloroform:Isoamyl Alcohol 25:24:1	Sigma	Cat#P2069

Sodium Acetate	Sigma	Cat#S2889
Freeze 'N Squeeze gel extraction column	Biorad	Cat#7326165
PMSF	Sigma	Cat#P7626
Sytox Green	Invitrogen	Cat#S7020
Raffinose	Sigma	Cat#R0250
ThruPLEX DNA-seq Kit	ThruPLEX DNA-seq Kit	Cat# R400674
Tween 20	Sigma	Cat#P9416
Triton X100	Sigma	Cat#T8787
Phenol-Chloroform 5:1	Sigma	Cat#P1944-100ml
Chloroform:Isoamyl Alcohol 24:1	Sigma	Cat#C0549-1PT
Superscript IV reverse transcriptase	Life Technologies	Cat#18090050
TruSeq stranded total RNA	Illumina	Cat# 20020598
Random Hexamers	Life Technologies	Cat#N8080127
100mM dNTP set	Life Technologies	Cat#10297-018
RiboMinus Eukaryote Kit for RNA-seq	Ambion	Cat#A1083708
H2O sterile	Sigma	Cat#W3500
Benzonase	Sigma	Cat#E1014
Phosphatase inhibitor PhosStop	Sigma	Cat#4906837001
Concanavalin A	Sigma	Cat# L7647-25MG
Grace Bio-Labs SecureSeal	Sigma	Cat#GBL654006-100EA
Microscope Cover Glasses 1.5H 18x18mm	Zeiss	Cat#019030091
Paraformaldehyde 16%	VWR	Cat# 43368.9M
Deposited Data		
Deep sequencing data	N/A	GEO:GSE148170 and GSE136605 SRA: SRP125409 and SRP189465
Unprocessed gel images presented in this manuscript	Mendeley data	http://dx.doi.org/10.17632/3typz6j2hk.1
Experimental Models: Organisms/Strains		
All <i>S. cerevisiae</i> strains used in this study are listed in Table S5	N/A	N/A
Oligonucleotides		

All oligonucleotides used in this study are listed in Table S6	N/A	N/A
Software and Algorithms		
Prism	GraphPad	v7
Integrated Genome Browser (IGB)	https://bioviz.org/	v9
Bowtie2	N/A	N/A
Bamcompare	N/A	N/A
Bedtools	N/A	N/A
Samtools	N/A	N/A
R-studio_R	N/A	N/A
Galaxy_Deeptools2	N/A	N/A

Figure
Forey_Figure_1

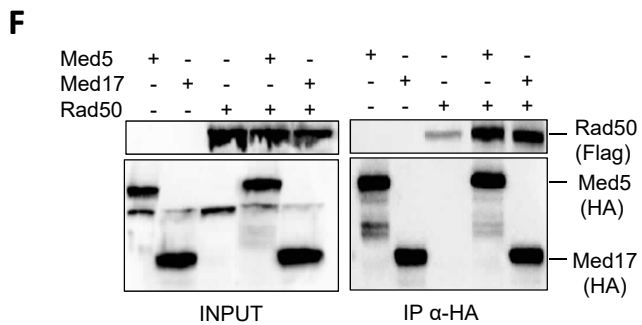
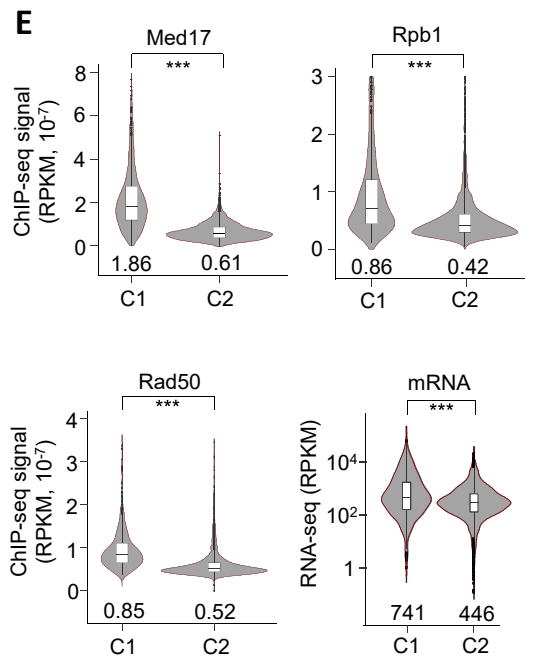
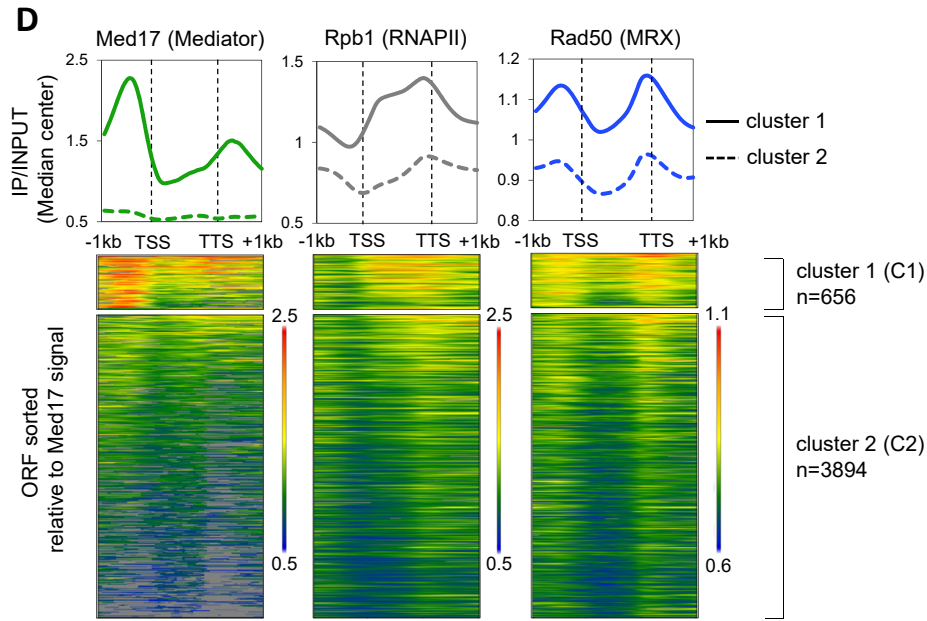
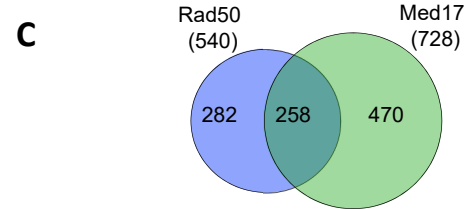
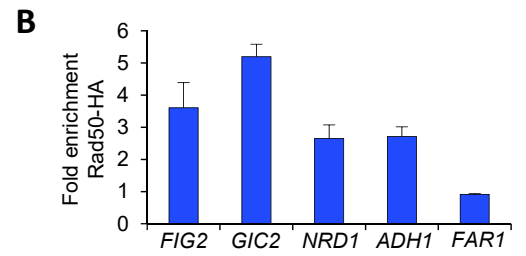
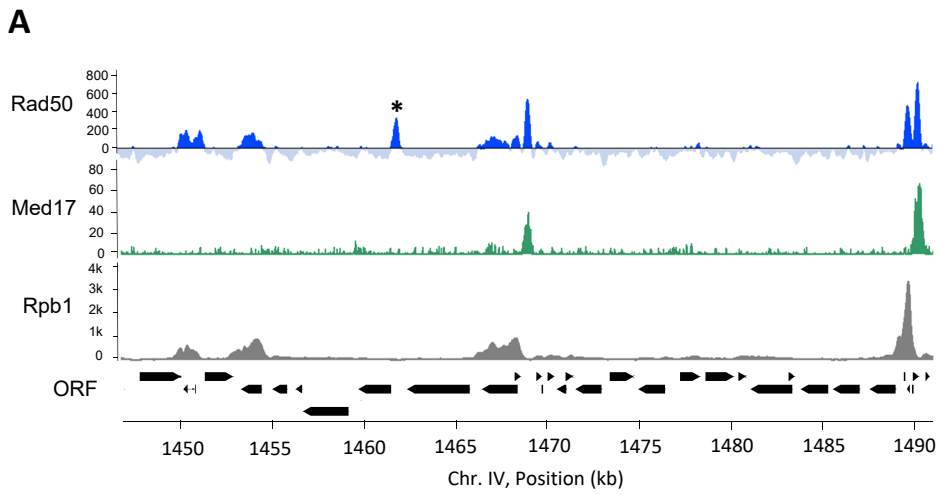


Figure
Forey_Figure_2

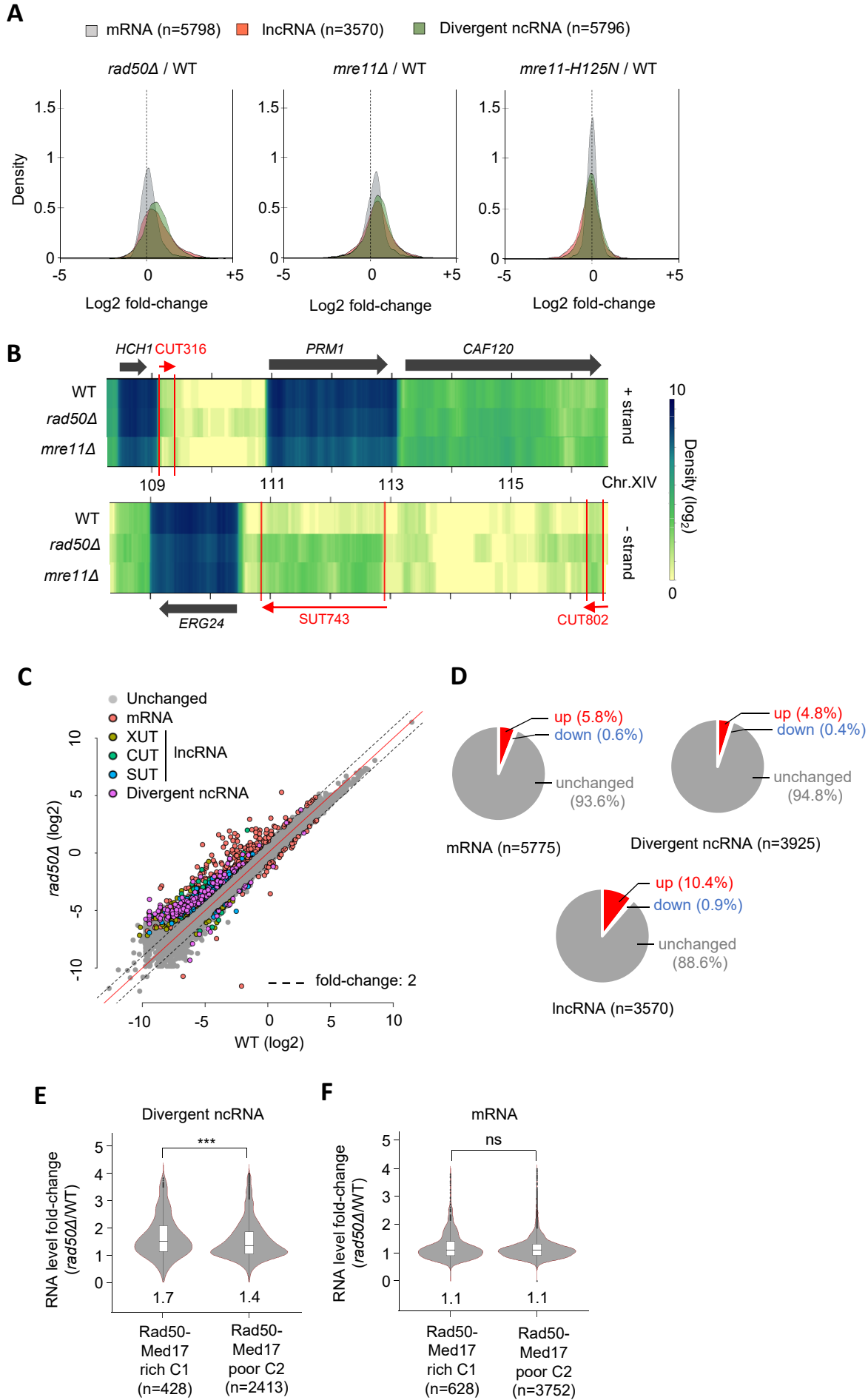


Figure
Forey_Figure_3

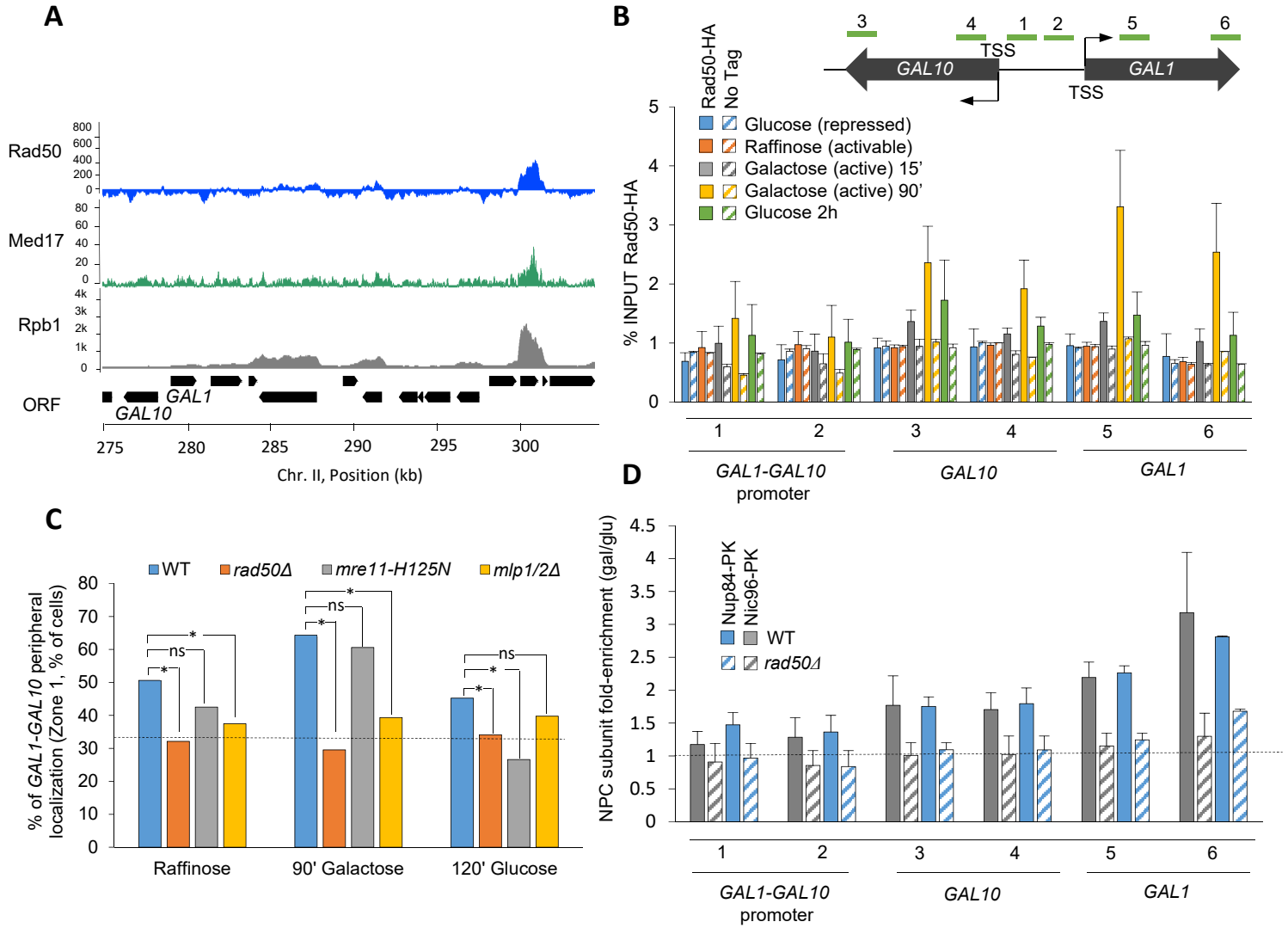


Figure
Forey_Figure_4

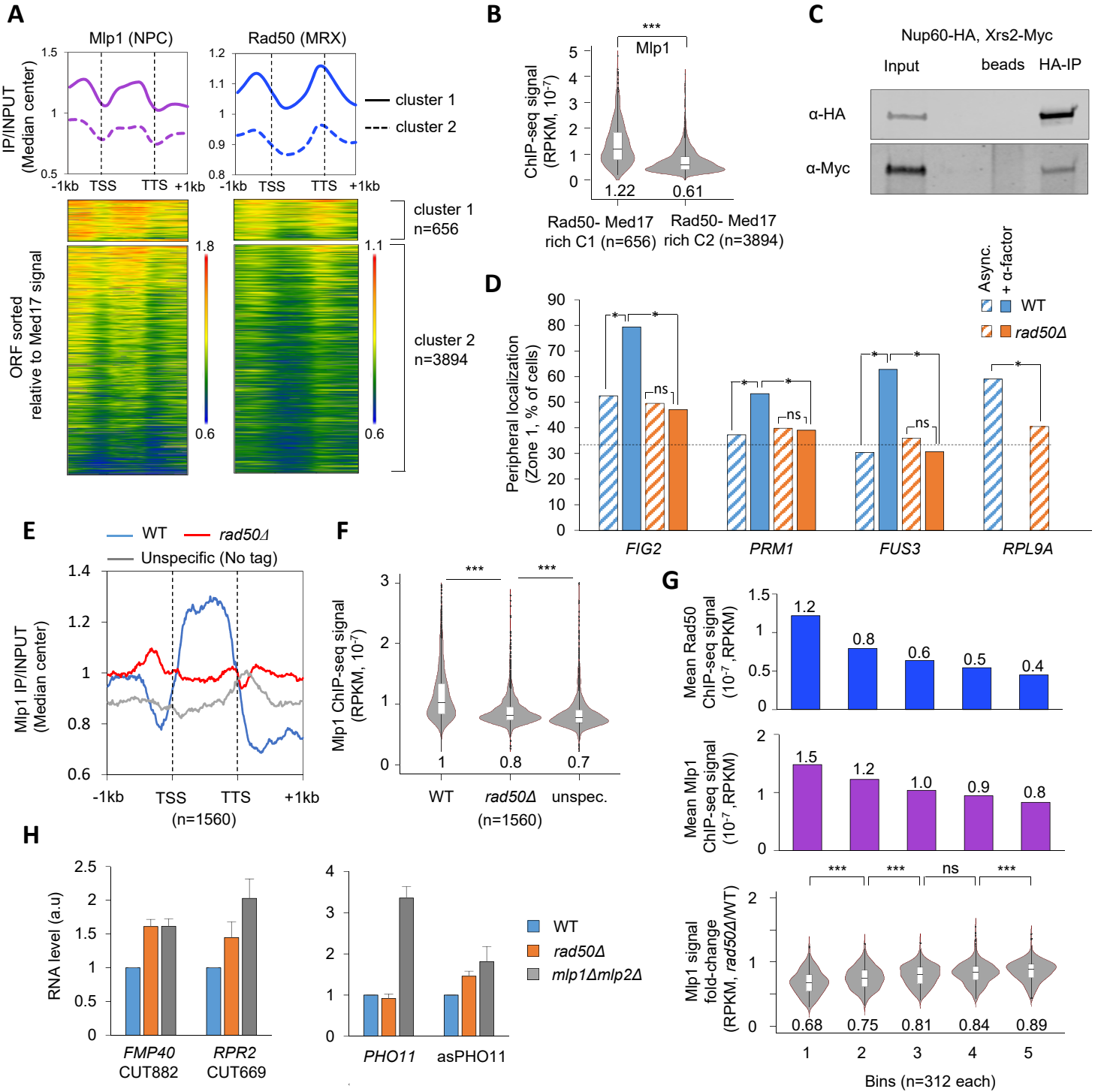


Figure
Forey_Figure_5

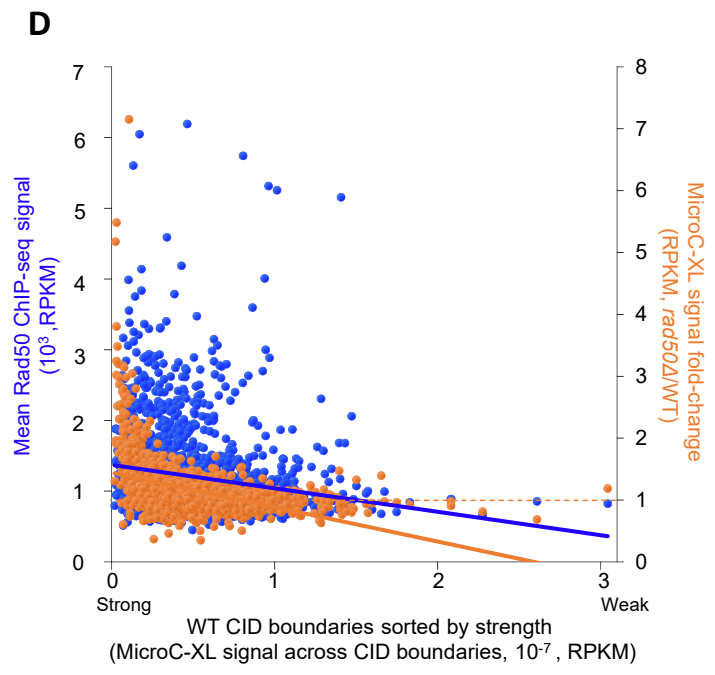
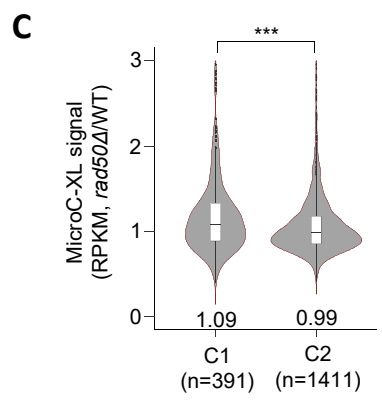
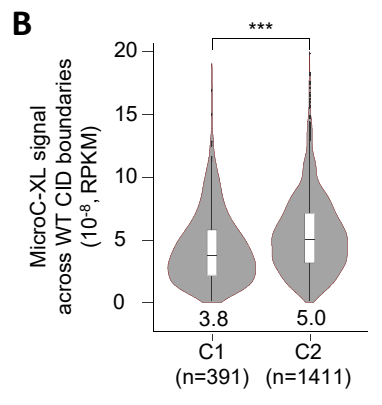
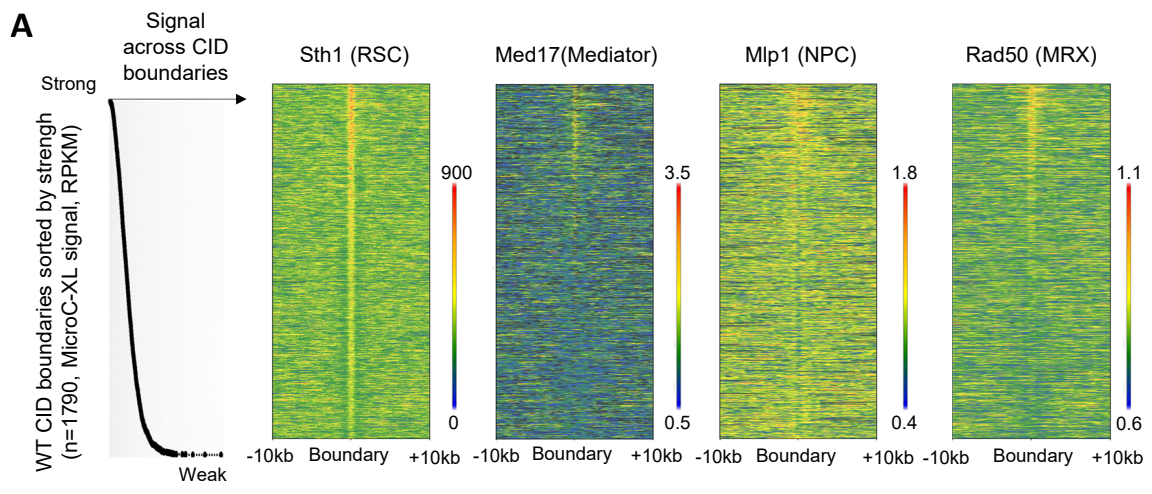
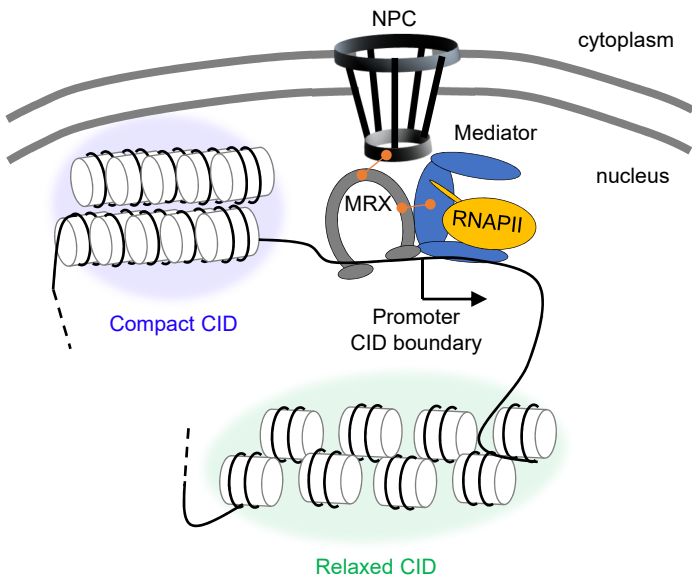
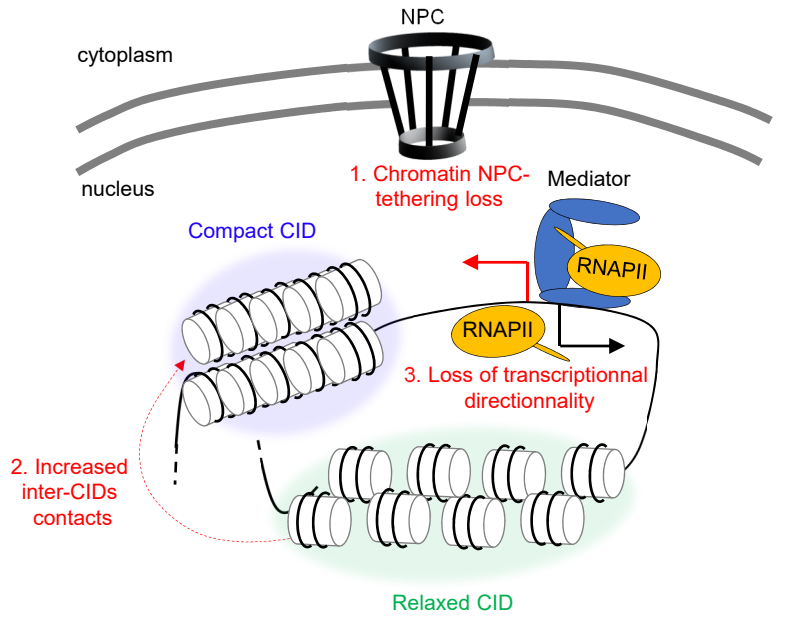


Figure
Forey_Figure_6

Wild-type



MRX mutants



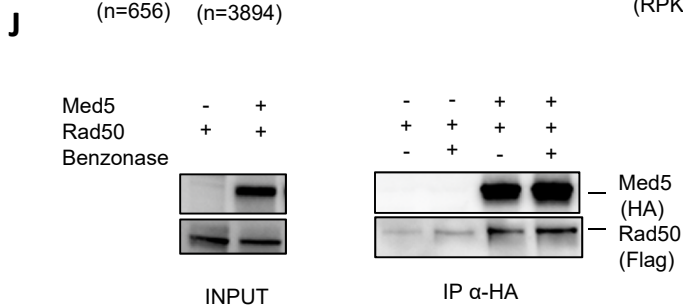
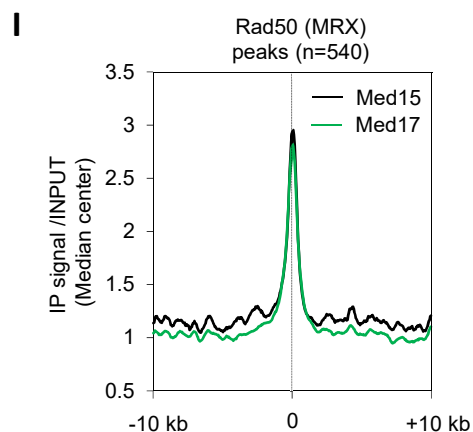
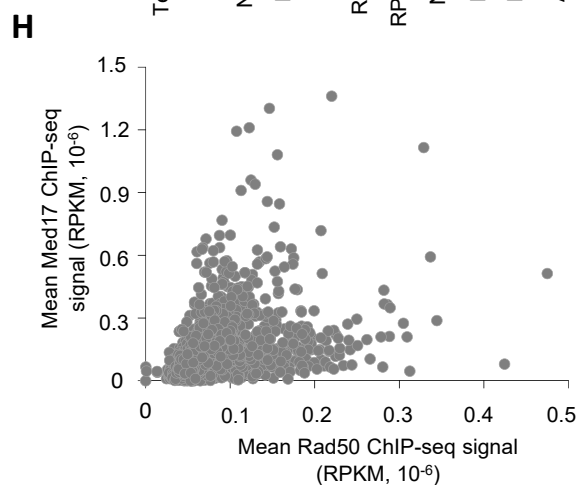
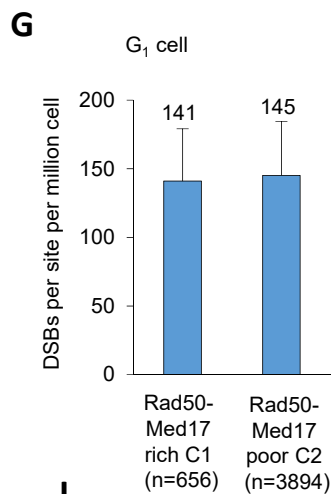
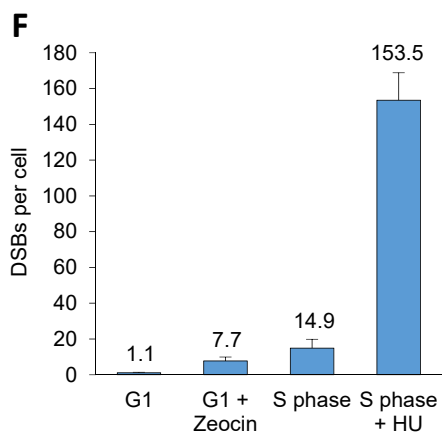
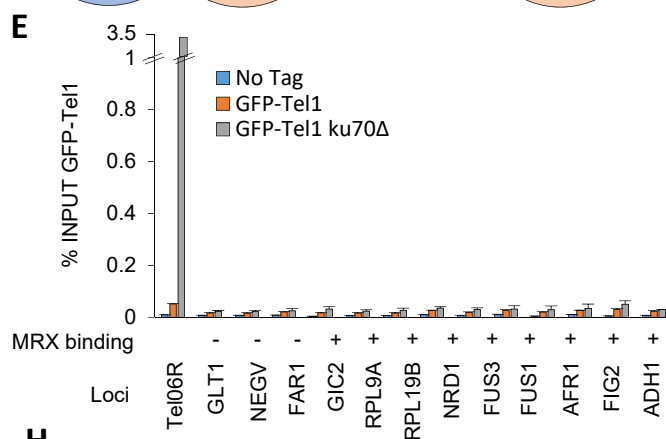
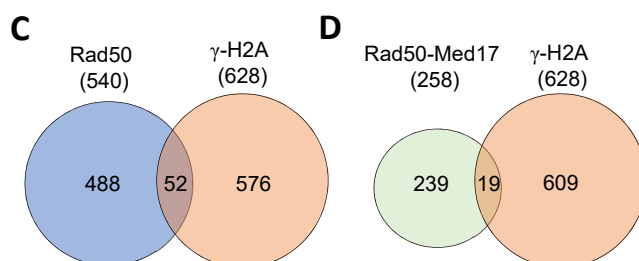
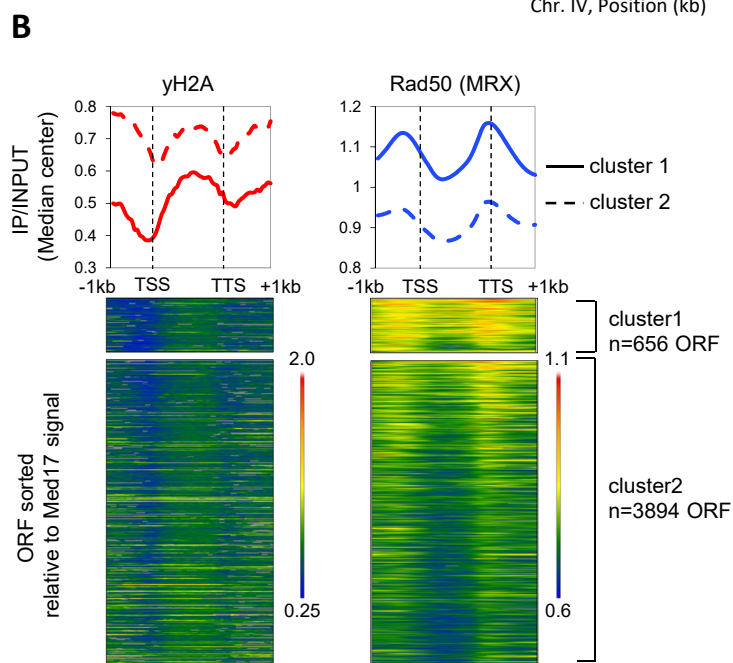
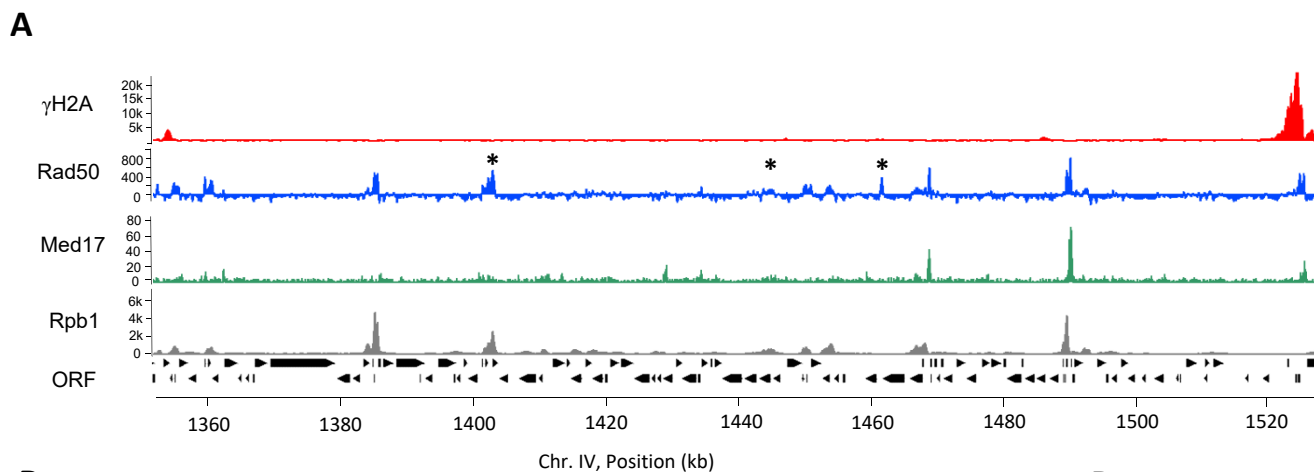


Figure S1. MRX binding to chromatin is distinct from spontaneous γ -H2A in G₁, Related to Figure 1.

(A) ChIP-seq browser plots on chromosome IV of γ -H2A (red, (Forey et al., 2020)), Rad50 (blue), Med17 (green, (Eyboulet et al., 2013)) and Rpb1 (grey) in wild-type strain synchronized in G₁ with α -factor (Rpb1 and Rad50) or asynchronous (Med17). Signals are expressed as a ratio of the corresponding protein over input DNA, and for Rad50 ChIP minus the signal obtained in unspecific IP (untagged strain). ORF are indicated in black. Peaks filtered out by MACS2 and loci prone to generate artifact (Teytelman, 2013) are indicated by asterisks.

(B) Heatmaps and average profiles of Rad50 and γ -H2A, from -1 kb from TSS to +1Kb to TTS. ORF were sorted and separated in two clusters (C1=656 and C2=3894 ORF, deeptools2 Kmeans clustering) based on the level of Med17 signal intensity.

(C-D) Venn diagram showing the overlap of Rad50 and γ -H2A peaks (at least 1 bp) or between Rad50-Med17 common peaks and γ -H2A peaks (at least 1 bp).

(E) GFP-Tel1 enrichment was assessed by ChIP-qPCR by measuring the level of Tel1 in wild-type and *ku70 Δ* cells synchronized in G₁ with α -factor. Data are expressed as a percentage of Input. MRX presence (+) or absence (-) at a given loci is indicated. Tel1 enrichment in *ku70 Δ* cells at telomere (Tel06R) is a positive control. Unspecific enrichment correspond to the IP values in an untagged strain (no tag). Error bars represent SEM of 2 biological replicates.

(F) Quantification of DNA breaks in quantitative bless in the indicated condition.

(G). Occurrence of DNA breaks per genomic location per cell in genes found in the Mediator-MRX-enriched cluster 1 or the Mediator-MRX-poor cluster 2.

(H) Scatter plot representing Med17-HA ChIP-seq enrichment (async. cells) versus Rad50-HA ChIP-seq enrichment (G₁ synchronized cells).

(I) Average profile of Med15 and Med17 (Eyboulet et al., 2013) centered on Rad50 (MRX) peaks (n=540).

(J) co-IP to test the interaction between Mediator and MRX including Benzonase treatment. Signals over background can be detected for Rad50-Flag in a Med5-HA in comparison to the same IP in a strain devoid of HA tag, and is not affected by Benzonase treatment.

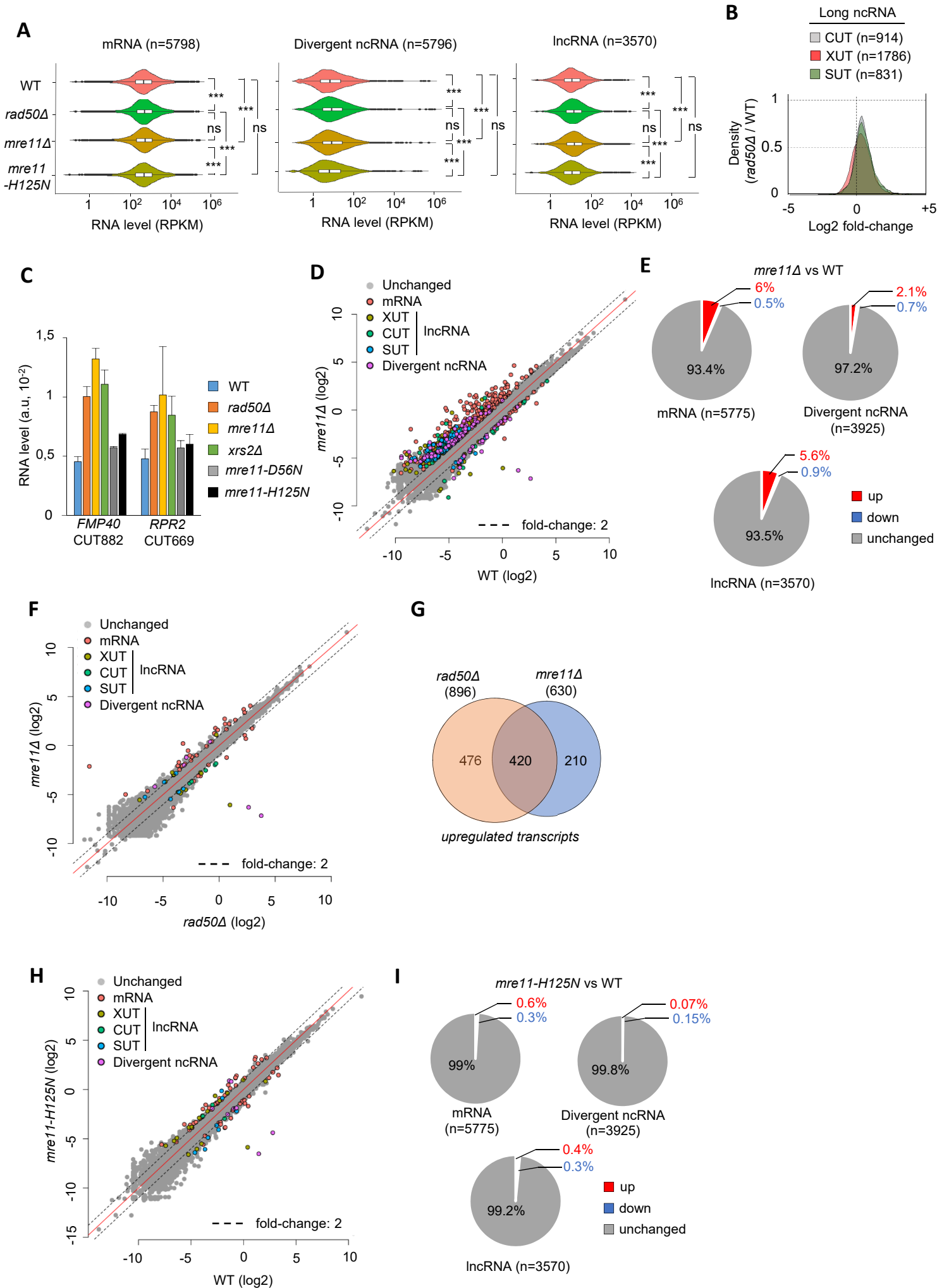


Figure S2. The MRX complex limits transcripts accumulation, Related to Figure 2.

(A) Violin plots of RNA-seq signals (RPKM) in WT, *rad50Δ*, *mre11Δ* and *mre11-H125N* cells for mRNA, divergent ncRNA and lncRNA. *** P -value $< 10^{-3}$, by two-sided Mann-Whitney paired test; ns, not significant.

(B) Density plot of RNA-seq signals expressed as a log₂ fold-change ratio for *rad50Δ* over wild-type cells showing the 3 classes of unstable long non-coding RNA including CUT (n=914), SUT (n=831) and XUT (n=1786).

(C) RNA level of CUT882 and CUT669 determined by RT-qPCR from total RNA and normalized over *ACT1*.

(D-F) Scatter plot of RNA-seq tag density (log₂) for mRNA (n=5639), divergent ncRNA (n=5213), lncRNA (CUT, SUT and XUT, n=3374) in WT versus *mre11Δ* cells (D) or *rad50Δ* versus *mre11Δ* cells (F). Transcripts differentially expressed between strains are circled in colors, unchanged transcripts are colored in grey.

(E) Pie charts illustrate the proportion of transcripts differentially expressed in *mre11Δ* versus WT.

(G) Venn diagram showing the overlap of transcripts upregulated in *rad50Δ* and *mre11Δ* versus WT.

(H) Scatter plot of RNA-seq tag density (log₂) for mRNA (n=5639), divergent ncRNA (n=5213), lncRNA (CUT, SUT and XUT, n=3374) in WT and *mre11-H125N* cells. Transcripts differentially expressed between *mre11-H125N* and WT are circled in colors, unchanged transcripts are colored in grey.

(I) Pie charts illustrate the proportion of transcripts differentially expressed in *mre11-H125N* versus WT.

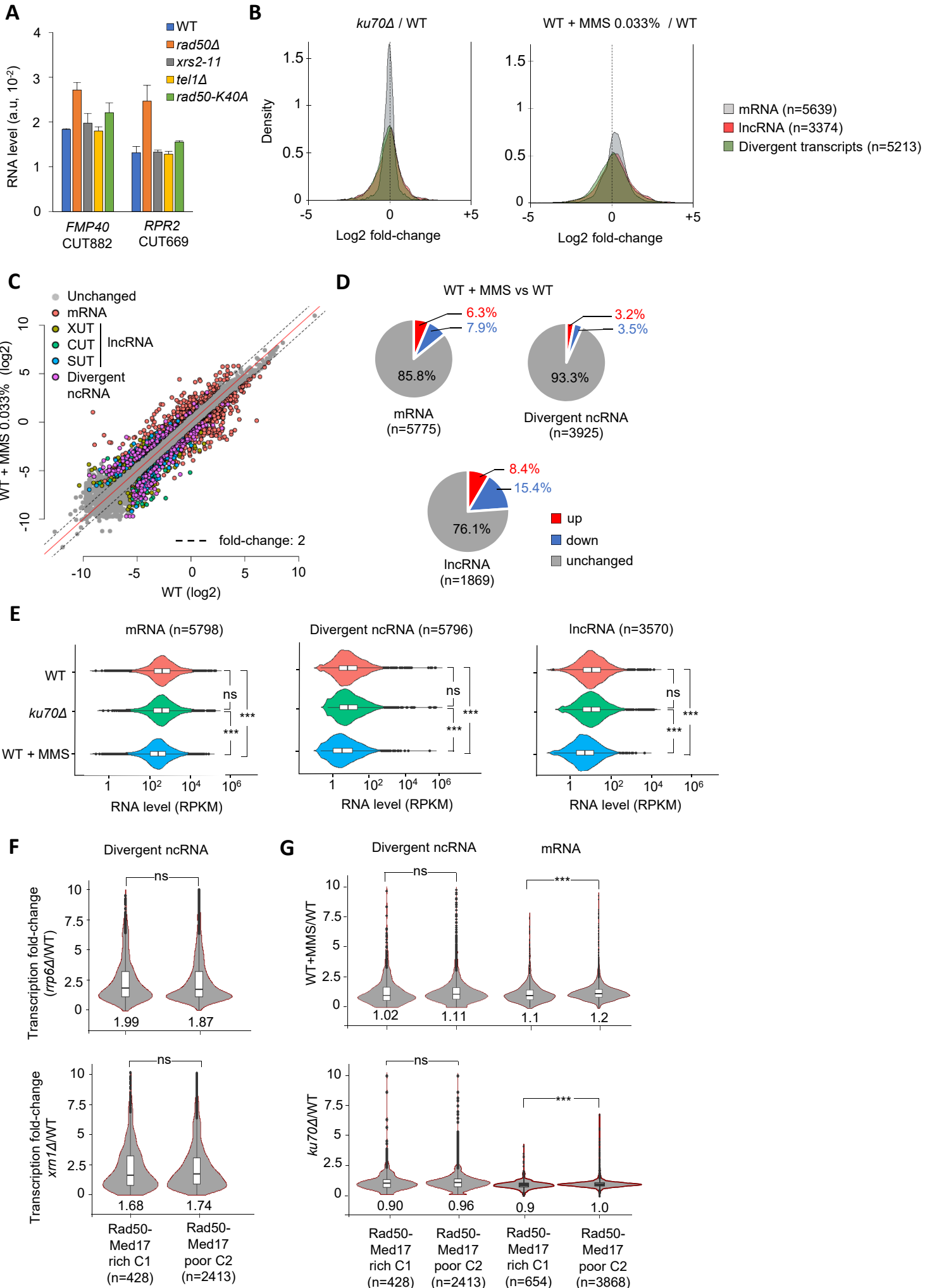


Figure S3. MRX repression defects is distinct from spontaneous damage or MMS-induced damage response, Related to Figure 2.

(A) RNA level of CUT882 and CUT669 determined by RT-qPCR from total RNA and normalized over *ACT1*.

(B) Density plots of RNA-seq signals expressed as a log₂ fold-change ratio for *ku70Δ* over WT cells, or WT treated for 60 min with MMS 0.033% cells over WT cells, for mRNA (grey, n= 5798), long non-coding RNA including CUT, SUT and XUT (red, n=3570) and divergent transcripts (green, n=5796).

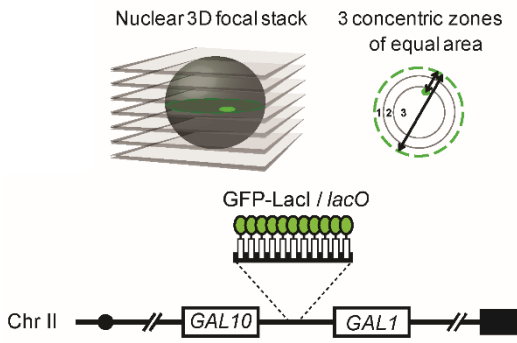
(C) Scatter plot of RNA-seq tag density (log₂) for mRNA (n=5639), divergent ncRNA (n=5213), lncRNA (CUT, SUT and XUT, n=3374) in WT versus WT + MMS 0.033% cells. Transcripts differentially expressed between WT + MMS 0.033% and WT are circled in colors, unchanged transcripts are colored in grey.

(D) Pie charts illustrate the proportion of transcripts differentially expressed in WT + MMS 0.033% versus WT.

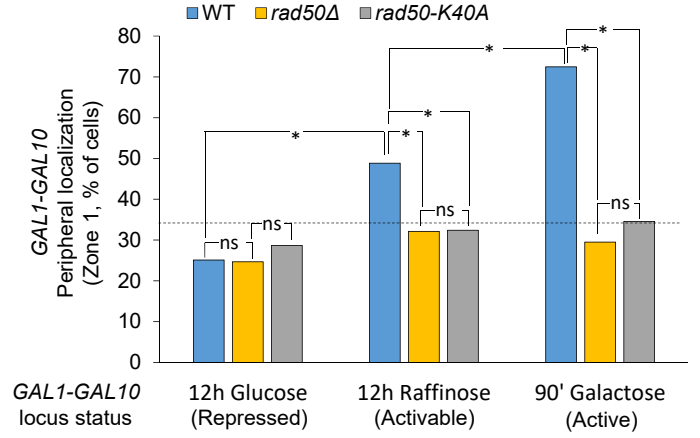
(E) Violin plots of RNA-seq signals (RPKM) in WT, *ku70Δ*, and WT + MMS 0.033% cells for mRNA, divergent ncRNA and lncRNA. *** *P*-value < 10⁻³, by two-sided Mann-Whitney paired test; ns, not significant.

(F-G) Violin plots of transcription fold-change in the indicated mutant/condition over the WT for mRNA, divergent ncRNA and lncRNA in either cluster. The median is indicated below each violin. *** *P*-value < 10⁻³, by two-sided Mann-Whitney paired test; ns, not significant.

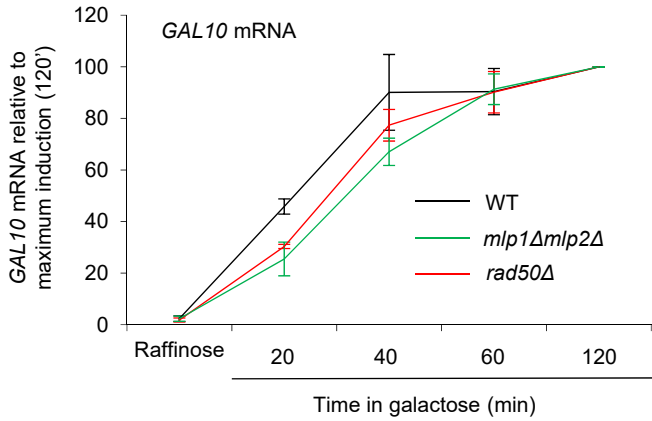
A



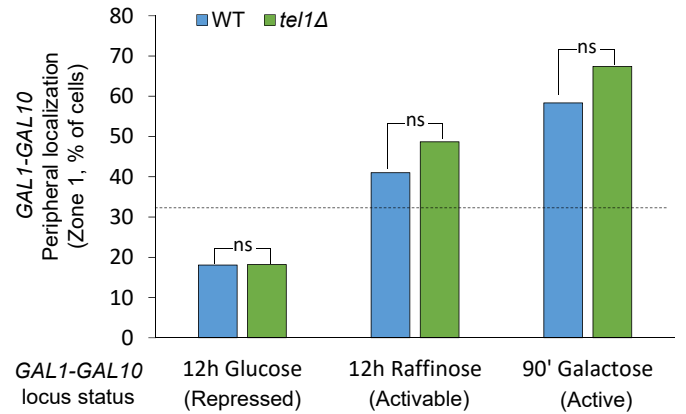
B



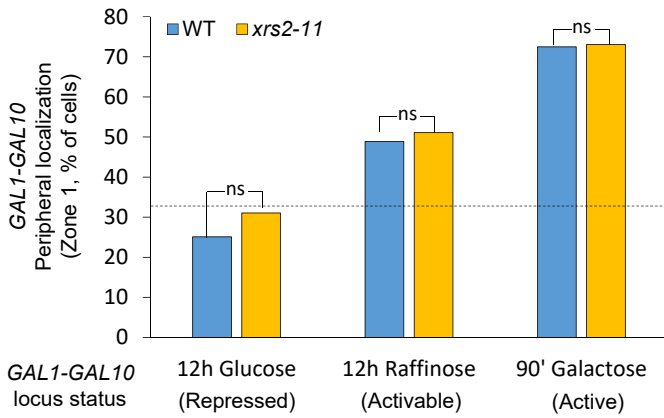
C



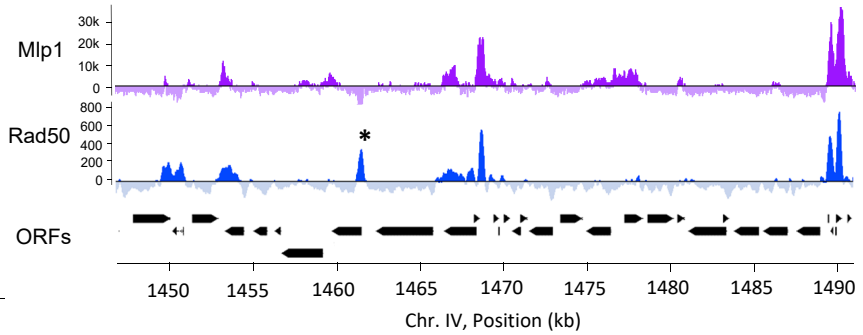
D



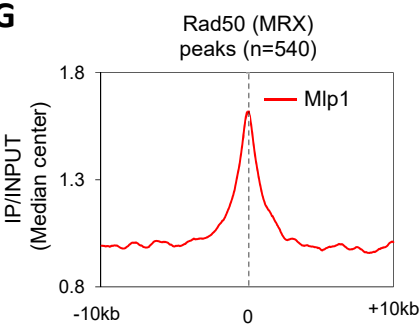
E



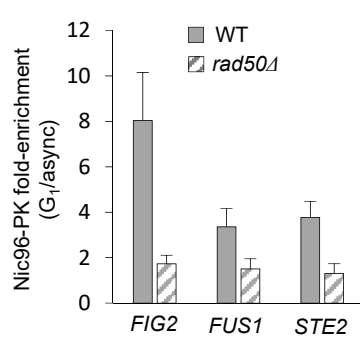
F



G



H



I

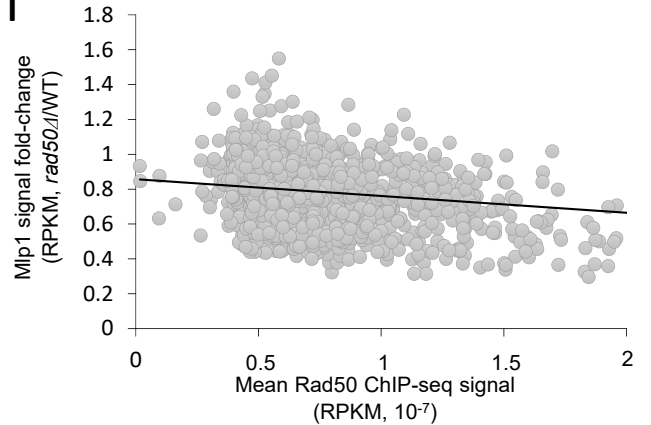


Figure S4. MRX mediates chromatin-NPC interactions, Related to Figure 4.

(A) LacO repeats were inserted upstream of *GAL1* in order to visualize the locus in the presence of LacI-GFP. Three zones of equal surface were defined. Zone 1 corresponds to the nuclear periphery and zone 3 to the center of the nucleus.

(B) Distribution of *GAL1-GAL10* locus in WT, *rad50Δ* and *rad50-K40A* strains when cells are grown in transcriptionally activable (raffinose), induced (galactose) or repressed (glucose) conditions. *** *P*-value < 10⁻³, by two-sided Fischer's Exact t-test; ns, not significant.

(C) RNA level of *GAL10* determined by RT-qPCR from total RNA and normalized over *ACT1* in WT, *mlp1/2Δ* and *rad50Δ* cells. Data are expressed as percentage of maximum induction measured at t=120' in presence of galactose.

(D-E) Distribution of *GAL1-GAL10* locus in WT, *tel1Δ* and *xrs2-11* strains when cells are grown in transcriptionally permissive (raffinose), induced (galactose) or repressed (glucose) conditions. *** *P*-value < 10⁻³, by two-sided Fischer's Exact t-test; ns, not significant.

(F) ChIP-seq browser plots on chromosome IV of Mlp1 (purple) and Rad50 (blue) in wild-type strain synchronized in G₁ with α-factor. Signals are expressed as a ratio of the corresponding protein over input DNA. The signal from an unspecific IP (untagged strain) was subtracted after the ratio IP/INPUT. ORF are indicated in black. Peaks filtered out by MACS2 and loci prone to generate artifact (Teytelman, 2013) are indicated by asterisks.

(G) Average profile of Mlp1 centered on Rad50 (MRX) peaks (n=540).

(H) Nic96-PK enrichment was assessed by ChIP-qPCR at several mating pheromone induced genes. Data are expressed as a ratio of induced (+ α-factor) over non-induced (asynchronous) conditions. Error bars represent SEM of 2 biological replicates.

(I) Scatter plot representing Mlp1 ChIP-seq signal fold-change (*rad50Δ*/WT) versus Rad50 ChIP-seq signal.

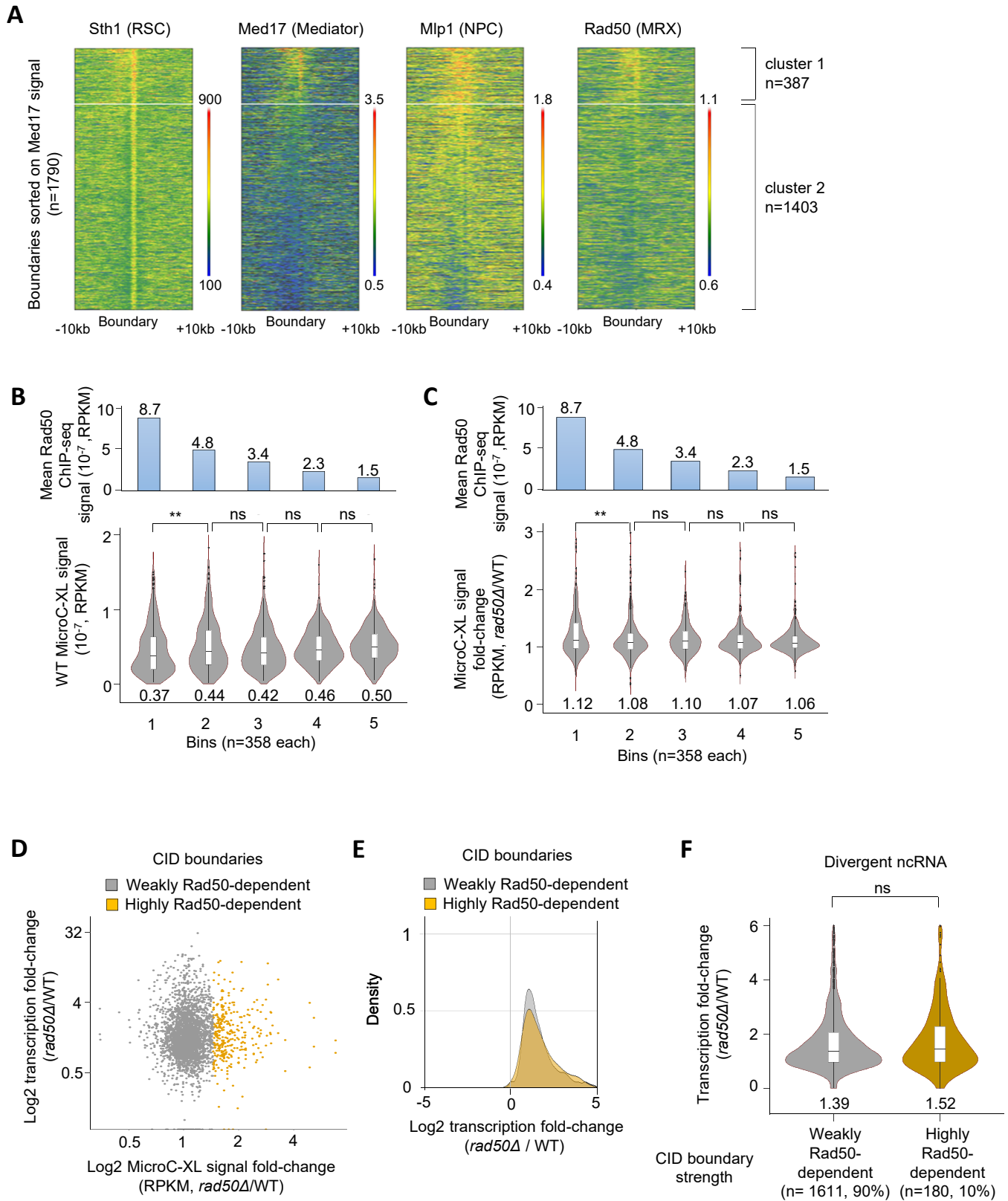


Figure S5. MRX promotes chromosomal interaction domains (CID) insulation, Related to Figure 5.

(A) Boundaries from MicroC-XL were assigned in ORF cluster 1 or 2 generated above on Med17 (Mediator) levels (as in Figure 1D). Data are expressed as a ratio of the corresponding protein over input DNA.

(B-C) Violin plots representing the wild-type MicroC-XL signals (B) or the MicroC-XL signal fold-change (*rad50Δ*/WT) (C) between adjacent CIDs through a given boundary in five bins define on Rad50 level at the boundary. The mean Rad50 level is indicated with a histogram in each bin. The median is indicated below each violin. *** P -value $< 10^{-3}$, by two-sided Mann-Whitney; ns, not significant.

(D) Scatter plot representing the divergent ncRNA level fold-change (*rad50Δ*/WT) versus the MicroC-XL across signal fold-change (*rad50Δ*/WT) across CID boundaries. The highly (orange, 10%, $n=180$) and weakly (grey, 90%, $n=1611$) Rad50-dependent CID boundaries for insulation strength are indicated.

(E) Density plots of RNA-seq signals expressed as a log₂ fold-change ratio for *rad50Δ* over WT cells for the highly and weakly Rad50-dependent CID boundaries.

(F) Violin plots of divergent ncRNA transcription fold-change (*rad50Δ*/WT) in highly and weakly Rad50-dependent CID boundaries. The median is indicated below each violin. ns, not significant by two-sided Mann-Whitney paired test.

Table S5. Yeast strains used in this study. Related to STAR Method.

Collection number	Full genotype
GA4098	<i>MATa, ade2-1, trp1-1, can1-100, leu2-3,112, his3-11,15, ura3, GAL, RAD5, NUP49-GFP his3-15::GFP-lacI::HIS3 GAL10::GAL10-lacOp-TRP1</i>
GA9649	<i>MATa, ade2-1, trp1-1, can1-100, leu2-3,112, his3-11,15, ura3, GAL, RAD5, rad50::KAN, NUP49-GFP,his3-15::GFP-lacI::HIS3 GAL10::GAL10-lacOp-TRP1</i>
GA9721	<i>MATa, ade2-1, trp1-1, can1-100, leu2-3,112, his3-11,15, ura3, GAL, RAD5, MLP1-eCFP</i>
GA9747	<i>MATa, ade2-1, trp1-1, can1-100, leu2-3,112, his3-11,15, ura3, GAL, RAD5, mre11::mre11-H125N, NUP49-GFP,his3-15::GFP-lacI::HIS3 GAL10::GAL10-lacOp-TRP1</i>
GA9750	<i>MATa, ade2-1, trp1-1, can1-100, leu2-3,112, his3-11,15, ura3, GAL, RAD5, mlp1::HIS3, mlp2::TRP1, NUP49-GFP,his3-15::GFP-lacI::HIS3 GAL10::GAL10-lacOp-TRP1</i>
GA9810	<i>MATa, ade2-1, trp1-1, can1-100, leu2-3,112, his3-11,15, ura3, GAL, RAD5, rad50::KAN, MLP1-eCFP</i>
PP1416	<i>MATa, ade2-1, trp1-1, can1-100, leu2-3,112, his3-11,15, ura3, GAL, RAD5, RAD50-HA6::TRP, URA3::GPD-TK7</i>
PP1502	<i>MATa, ade2-1, trp1-1, can1-100, leu2-3,112, his3-11,15, ura3, GAL, RAD5, rrp6::TRP, URA3::GPD-TK7</i>
PP1591	<i>MATa, ade2-1, trp1-1, can1-100, leu2-3,112, his3-11,15, ura3, GAL, RAD5, rad50::KAN, URA3::GPD-TK7</i>
PP1661	<i>MATa, ade2-1, trp1-1, can1-100, leu2-3,112, his3-11,15, ura3, GAL, RAD5, mre11::mre11-D56N</i>
PP1662	<i>MATa, ade2-1, trp1-1, can1-100, leu2-3,112, his3-11,15, ura3, GAL, RAD5, mre11::mre11-H125N</i>
PP1669	<i>MATa, ade2-1, trp1-1, can1-100, leu2-3,112, his3-11,15, ura3, GAL, RAD5, mre11::HIS</i>
PP1888	<i>MATa, ade2-1, trp1-1, can1-100, leu2-3,112, his3-11,15, ura3, GAL, RAD5, ku70::HIS</i>
PP1920	<i>MATa, ade2-1, trp1-1, can1-100, leu2-3,112, his3-11,15, ura3, GAL, RAD5, xrn1::ADE2</i>
PP2817	<i>MATa, ade2-1, trp1-1, can1-100, leu2-3,112, his3-11,15, ura3, GAL, RAD5, mlp2::HIS3, mlp1::TRP1</i>
PP2824	<i>MATa, ade2-1, trp1-1, can1-100, leu2-3,112, his3-11,15, ura3, GAL, RAD5, xrs2::HI</i>
PP3814	<i>MATa, ade2-1, trp1-1, can1-100, leu2-3,112, his3-11,15, ura3, GAL, psi+, RAD5, Nic96-PK9-HIS3</i>
PP3815	<i>MATa, ade2-1, trp1-1, can1-100, leu2-3,112, his3-11,15, ura3, GAL, psi+, RAD5, Nup84-PK6-KAN</i>
PP3840	<i>MATa, ade2-1, trp1-1, can1-100, leu2-3,112, his3-11,15, ura3, GAL, psi+, RAD5, Nic96-PK9-HIS3, rad50::KAN</i>
PP3847	<i>MATa, ade2-1, trp1-1, can1-100, leu2-3,112, his3-11,15, ura3, GAL, psi+, RAD5, Nup84-PK6-KAN, rad50::KAN</i>
PP3939	<i>MATa can1Δ::pSTE2-spHIS5 lyp1Δ his3Δ1 leu2Δ0 ura3Δ0 NDC1::NDC1-tomato::NatMx6::CFP-NLS::LacI-GFP ybl012cΔ::LacO256::LEU2</i>
PP3943	<i>MATa-inc, ADH4cs::HIS2 ade1 his2 leu2 trp1 ura3</i>
PP3945	<i>MATa-inc, ADH4cs::HIS2 ade1 his2 leu2 trp1 ura3, xrs2-11::KanMX</i>

PP3947	<i>MATa, ade2-1, trp1-1, can1-100, leu2-3,112, his3-11,15, ura3, GAL, psi+, RAD5, tel1::HYG</i>
PP3948	<i>MATa, ade2-1, trp1-1, can1-100, leu2-3,112, his3-11,15, ura3, GAL, psi+, RAD5, tel1::HYG</i>
PP3950	<i>Mat a, ade2, his3, leu2, trp1, ura3, Nup49-GFP, LacI-GFP-HIS3, GAL10-LacO-TRP1, tel1::HYG</i>
PP3952	<i>MATa, ade2-1, trp1-1, can1-100, leu2-3,112, his3-11,15, ura3, GAL, psi+, RAD5, yEGFP-TEL1</i>
PP3964	<i>MATa, MATα can1Δ::pSTE2-spHIS5 lyp1Δ his3Δ1 leu2Δ0 ura3Δ0 met15Δ0 NDC1::NDC1-tomato::NatMx6::CFP-NLS::LacI-GFP FIG2::LacO256::LEU2</i>
PP3965	<i>MATa, can1Δ::pSTE2-spHIS5 lyp1Δ his3Δ1 leu2Δ0 ura3Δ0 met15Δ0, NDC1::NDC1-tomato::NatMx6::CFP-NLS::LacI-GFP FIG2::LacO256::LEU2 ; rad50::KAN</i>
PP3967	<i>MATa can1Δ::pSTE2-spHIS5 lyp1Δ his3Δ1 leu2Δ0 ura3Δ0 NDC1::NDC1-tomato::NatMx6::CFP-NLS::LacI-GFP ybl012cΔ::LacO256::LEU2 ; rad50::KAN</i>
PP3968	<i>MATa can1Δ::pSTE2-spHIS5 lyp1Δ his3Δ1 leu2Δ0 ura3Δ0 NDC1::NDC1-tomato::NatMx6::CFP-NLS::LacI-GFP RPL9A::LacO256::LEU2</i>
PP3969	<i>MATa can1Δ::pSTE2-spHIS5 lyp1Δ his3Δ1 leu2Δ0 ura3Δ0 NDC1::NDC1-tomato::NatMx6::CFP-NLS::LacI-GFP RPL9A::LacO256::LEU2 ; rad50::KAN</i>
PP3983	<i>MATa, ade2-1, trp1-1, can1-100, leu2-3,112, his3-11,15, ura3, GAL, psi+, RAD5, yEGFP-TEL1, ku70::HIS</i>
PP3985	<i>Mat a, TRP1:pGPDmCherry-ER04 HIS3:LacI-GFP PRM1:URA3p6LacO128 ; rad50::KAN</i>
PP3986	<i>MATa-inc, ADH4cs::HIS2 ade1 his2 leu2 trp1 ura3, LacI-GFP-HIS3, Nup49-GFP, GAL10-LacO-TRP1</i>
PP3988	<i>MATa-inc, ADH4cs::HIS2 ade1 his2 leu2 trp1 ura3, xrs2-11::KanMX, LacI-GFP-HIS3, Nup49-GFP, GAL10-LacO-TRP1</i>
PP4045	<i>Mat a, ade2, his3, leu2, trp1, ura3, hmlD::ADE1, hmrD::ADE1, RAD50-K40A::HYG</i>
PP4049	<i>Mat a, ade2, his3, leu2, trp1, ura3, LacI-GFP-HIS3, Nup49-GFP, GAL10-LacO-TRP1, RAD50-K40A::HYG</i>
PP870	<i>MATa, ade2-1, trp1-1, can1-100, leu2-3,112, his3-11,15, ura3, GAL, RAD5</i>
Y5871	<i>MATa ura3-52 his3-Δ200 ade2-101uaa trp1-Δ63 lys2-801uag leu2-Δ1 MED17::3HA::HIS3 med7::KanMX6 MED7 CEN TRP1</i>
Y5895	<i>MATa ura3-52 his3-Δ200 ade2-101uaa trp1-Δ63 lys2-801uag leu2-Δ1 Med5::3HA::HIS3 med7::KanMX6 MED7 CEN TRP1</i>
Y7706	<i>MATa ura3-52 his3-Δ200 ade2-101uaa trp1-Δ63 lys2-801uag leu2-Δ1 MED5::3HA::HIS3 RAD50::3Flag::HPH med7::KanMX6 MED7 CEN TRP1</i>
Y7719	<i>MATa ura3-52 his3-Δ200 ade2-101uaa trp1-Δ63 lys2-801uag leu2-Δ1 MED17::3HA::HIS3 RAD50::3Flag::HPH med7::KanMX6 MED7 CEN URA3</i>
Y7925	<i>MATa ura3-52 his-Δ200 ade2-101uaa trp1-Δ63 lys2-801uag leu2-Δ1 RAD50::3Flag::HPH med7::KanMX6 MED7 CEN URA3</i>
yKD1231	<i>Mata-inc ade1 leu2-3,112 lys5 trp1::hisG ura3-52 hml::ADE1 hmr::ADE1 ade3::GALHO NUP60-6HA-KanMX4 XRS2-9myc-HPH</i>

Table S6. Oligos used in this study. Related to STAR Method.

Name	Sequence	Usage
ADH1_low_1	GTT GAT TGT ATG CTT GGT ATA GCT TG	ChIP-qPCR
ADH1_up_1	TTC CTT CCT TCA TTC ACG CAC ACT	ChIP-qPCR
AFR1-Pr-F	ACTCAAAAAGGAAATGCATGG	ChIP-qPCR
AFR1-Pr-R	GATGGGCACTCACTTTTCCT	ChIP-qPCR
anti-Pho11-Fw	GGCGAAACTGAGCTTGAATC	RT-qPCR
anti-Pho11-Rv	TTGCCAAATTGGTCATCTCA	RT-qPCR
FAR1-Pr-F1	CAAACGAAACTCTTGTTGGTGT	ChIP-qPCR
FAR1-Pr-R1	ATCCACTGGAAAGCTTCGTG	ChIP-qPCR
FIG2-Pr-F	CCTTATGCTCACTATTTCCGATT	ChIP-qPCR
FIG2-Pr-R	TCTTAATCTTAACGTTCCATTGTAGC	ChIP-qPCR
FMP40-down	CAATTCGGCTCATTTGCTGCACAGC	RT-qPCR
FMP40-Up	GGTTGAAGTTACCCAAGCGGATCC	RT-qPCR
FUS1-M-F	TTTCGTTAGACCCCAAAGTGA	ChIP-qPCR
FUS1-M-R	ACAGGAATGCATCCACAACCT	ChIP-qPCR
FUS3_pr_F1	GCTAGTTCGTTTGAAGTACAAGGA	ChIP-qPCR
FUS3_pr_R1	TCTTTGGCATATTATTTTCTTTCTT	ChIP-qPCR
GAL1_gene_F	TGAACGAGTCTCAAGCTTCTTGC	ChIP-qPCR
GAL1_gene_R	TGGAACCAAGTGAACAGTACAACCA	ChIP-qPCR
GAL1_ter_F	GATATGCTTTCAACCGCTGC	ChIP-qPCR
GAL1_ter_R	TGCATCTCGTCAGTTGGC	ChIP-qPCR
GAL10_1137_F	TGCCGGCACCAGATTTCAAG	ChIP-qPCR
GAL10_1184_R	GTCCGTTCACTTTCAAGTCAACAA	ChIP-qPCR
GAL10_ter_F	AGTGTCACAGCGAATTTCTCTC	ChIP-qPCR
GAL10_ter_R	TTGCTACCGTCCATATCTTTCC	ChIP-qPCR
GAL1pr-150F	TGAAAGTTCCAAAGAGAAGGTTTT	ChIP-qPCR
GAL1pr-150R	GGAAATGTAAAGAGCCCCATT	ChIP-qPCR
GAL1pr-185F	GGTTATGCAGCTTTTCCATTT	ChIP-qPCR
GAL1pr-185R	CGAATCAAATTAACAACCATAGGA	ChIP-qPCR
GIC2-Pr-F2	GCAAACACGAATTGATCACG	ChIP-qPCR
GIC2-Pr-R2	GAGGAAACGCTGCCGTTA	ChIP-qPCR
GLT1-F	TTTGACCCAGCACATGTTA	ChIP-qPCR
GLT1-R	GGGTGTGGAGTTTGTGGTCT	ChIP-qPCR
NEG_R	TCGCAGGAGCATATTTCTGTA	ChIP-qPCR
NEGV_F	GCACTTAATTGGCGTAAGCTG	ChIP-qPCR
Nrd1_TATA_F1	GGTGATTTATTGGTCATTACATACGGTACAT	ChIP-qPCR
Nrd1_TATA_R1	CAATACGATAATACGATGCGATACGATACG	ChIP-qPCR
Pho11-Fw	CATTCGTGACACCAAAAACCT	RT-qPCR
Pho11-Rv	CATATTGCGCCAAGAAATCA	RT-qPCR
RPL19B_5-F	GGGACTGGCCCTTCTTTCTA	ChIP-qPCR
RPL19B_5-R	CGATTTGGTGAAAAGATCTATCAAG	ChIP-qPCR
RPL9A_pr_F1	GAAGTGCAGGAGGTCAGAGG	ChIP-qPCR
RPL9A_pr_R1	TGATTTCAGAAGCTTTTACACACTAA	ChIP-qPCR
RPR2-down	GCCATCAGAGGGTTAGAAACACCTATTGTAAG	RT-qPCR
RPR2-Up	GACTCGAGCTCAGTGAGCCGTTTATTATTAC	RT-qPCR

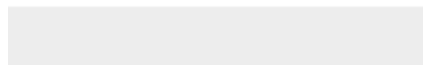
Tel06R-F	GTGTGTAGTGATCCGAACTCA	ChIP-qPCR
Tel06R-R	GCATATTGATATGGCGTACGCACACGT	ChIP-qPCR
GAL 10 Forward mid	TCTGCAAAGCTTCTGGTATTGA	RT-qPCR
GAL10 Reverse mid	AGCCGTCAAGTTCAAAACATC	RT-qPCR

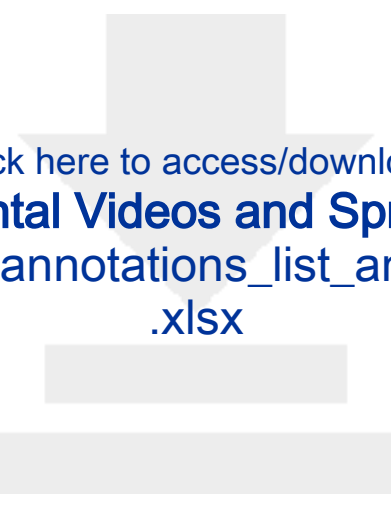


[Click here to access/download](#)

Supplemental Videos and Spreadsheets

TableS1_MRX_peaks.xlsx

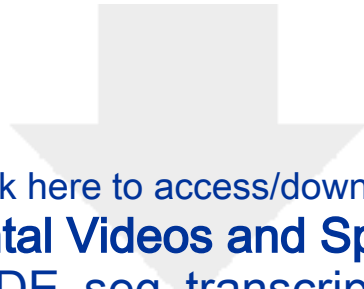




Click here to access/download

Supplemental Videos and Spreadsheets

TableS2_Clusters_annotations_list_and_GO_enrichment
.xlsx



[Click here to access/download](#)

Supplemental Videos and Spreadsheets
TableS3_DE_seq_transcripts_list.xlsx





[Click here to access/download](#)

Supplemental Videos and Spreadsheets
TableS4_DE_seq_GO_enrichment.xlsx

